Exploring Topographic Effects on Surface Parameters Over Rugged Terrains at Various Spatial Scales

Hanyu Shi, *Student Member, IEEE*, and Zhiqiang Xiao, *Member, IEEE*

***Abstract*— Topography is an inevitable factor when processing remote sensing data. Slope and aspect are sufficient for describing topographic conditions within a fine-scale pixel (e.g., 30 m); the resulting schematic is referred to as a sloping terrain and is modeled as a solo slope. A composite slope, which contains many solo slopes that are collectively referred to as rugged terrain, is needed for coarse-scale pixels (e.g., 1 km). However, many parameter estimation algorithms use topographic approximation methods, such as the assumption of a flat surface, assumption of a solo slope, omission of contributions from adjacent slopes, and usage of the terrain view factor (TVF) to approximate adjacent contributions. These topographic approximations can induce significant errors over mountain areas; however, errors caused by various approximation methods have not been comprehensively analyzed. This study summarizes radiative transfer (RT) processes over rugged terrains, proposes composite-slope models for surface parameters, and analyzes the influences of different topographic approximation methods on surface reflectance (ρ), directional brightness temperature (T_b), surface net radiation (E_n), slope downward radiation (E_d), absorbed photosynthetically active radiation (APAR), total emitted solar-induced chlorophyll fluorescence (SIF) by all leaves (F_e), SIF observed at the top of the canopy (F_o), broadband albedo (α), and broadband hemispherical emissivity (ε) at a series of spatial resolutions (30, 90, 270, 540, 1080, and 5400 m). Three surface types are tested: vegetation, soil, and snow. The results demonstrate that: 1) assumptions of a flat surface or a solo slope and the use of the TVF method induce significant errors (1%–58%) in all aforementioned parameters; 2) adjacent contributions can be neglected when simulating ε, APAR, F_o, F_e, and low-reflective ρ; and 3) adjacent contributions should be considered for E_n, E_d, and high-reflective ρ, and they are also significant when simulating α using fine-resolution data or over snow surfaces. These findings and the composite-slope models developed in this study benefit those who intend to conduct forward modeling and parameter estimation studies over rugged terrains.**

***Index Terms*— Adjacent effects, radiative transfer (RT), rugged terrain, solar-induced chlorophyll fluorescence (SIF), terrain radiation, topography.**

I. Introduction

REMOTE sensing is the only way to monitor the earth system on a global scale. Satellite observations, such as the 1-km Advanced Very High Resolution Radiometer (AVHRR) and the 500-m MODerate Resolution Imaging Spectroradiometer (MODIS), have provided data support for various studies in recent decades. With the advancement of sensor techniques, an increasing number of high spatial resolution satellite observations (e.g., 30-m Landsat and 10-m Sentinel) have become available in recent years. Simultaneously, studies on the effects of topography on surface parameters have received great interest since this effect is inevitable for high spatial resolution data.

The topography changes the incoming and outgoing radiation of targeted pixels through three aspects [1], [2]: 1) topography alters sun-target-sensor geometries, and thus, the direct radiation received by a pixel is changed; 2) the incoming (from the sky) and outgoing diffuse irradiance from a pixel are different from those over flat surfaces due to the obstruction of surrounding topography; and 3) the radiation reflected/emitted from adjacent pixels to a target pixel is another source of diffuse radiation, referred to as terrain radiation. Consequently, the observed radiance over a terrain surface is also different from that over a flat surface, and this difference causes errors in parameter estimation when ignoring the effect of topography. Many studies have demonstrated that ignoring topographic effects induces significant errors in the estimation of surface reflectance [3]–[5], surface temperature [6]–[8], surface long-wave and short-wave radiation [9]–[13], surface albedo [14], [15], and biophysical vegetative variables [16]–[18]. Therefore, introducing topography into remote sensing models and parameter estimation algorithms is essential to characterize earth properties accurately.

Topography modeling can be classified into solo-slope and composite-slope modelings according to the size of the target pixel [19]. For fine-scale pixels (e.g., 30 m), a single slope surface, or a solo slope, may be good enough to represent terrain conditions. The term "solo slope" is used to emphasize the topographic characteristic of a pixel. It also indicates that the spatial resolution of the digital elevation model (DEM) used is the same as the sensor's resolution. In contrast, a composite slope indicates that the pixel is large (e.g., 1 km). It covers many solo slopes, and a DEM, the spatial resolution of which is (much) finer than the sensor's resolution, is needed to describe the terrain conditions precisely. Composite-slope modeling is an inherent upscaling procedure [19]. Surface variables at a fine-resolution scale (i.e., solo slope) are firstly calculated; then, the corresponding variables at coarse-resolution

Manuscript received June 5, 2021; revised July 8, 2021; accepted July 16, 2021. This work was supported by the National Natural Science Foundation of China under Grant 41771359. *(Corresponding author: Zhiqiang Xiao.)*

The authors are with the State Key Laboratory of Remote Sensing Science, Faculty of Geographical Science, Beijing Normal University, Beijing 100875, China (e-mail: shihanyu@mail.bnu.edu.cn; zhqxiao@bnu.edu.cn).

This article has supplementary downloadable material available at https://doi.org/10.1109/TGRS.2021.3098607, provided by the authors.

Digital Object Identifier 10.1109/TGRS.2021.3098607

scales (i.e., composite slope) can be generated using upscaling procedures. The accuracy of the solo-slope model determines the accuracy of the composite-slope model.

Most terrain models have been developed for solo slopes. Based on radiative transfer (RT) and/or geometric optical (GO) theories, several studies have developed various forward models for simulating sensor observations over terrain surfaces [2], [20]–[27]. In addition to these models for simulating sensor observations, terrain models for estimating surface albedo [5], [28], surface radiation [10], [29]–[32], solar-induced chlorophyll fluorescence (SIF) [33], and the fraction of absorbed photosynthetically active radiation (FAPAR) [18] have also been developed. Among these studies, topographic effects on direct and diffuse radiation are well modeled. However, terrain radiation is usually neglected or modeled through approximation algorithms. The reasons for neglecting terrain radiation are: 1) its contributions are usually small except over highly reflective surfaces or in areas with deep valleys [2], [8], [34], [35] and 2) the calculation of terrain radiation can be computationally expensive when using fine-resolution (e.g., 30 m) DEM. The Proy algorithm [1], which is a radiosity method [36], has been widely used to calculate terrain radiation and proven very accurate [2], [8], [12], [13], [36]–[38]. However, for each pixel, this algorithm requires calculating contributions from surrounding pixels within a search radius (e.g., 0.5–1.5 km), and the visibility (0 or 1) between any two pixels is also needed to be calculated. What is more, this process has to be iterated until reaching a convergence point (e.g., the difference between two iterations is less than 0.1%). Therefore, it takes a long time to simulate terrain radiation for fine-resolution DEM using the accurate Proy algorithm [2]. The detailed calculation process of terrain radiation using the Proy algorithm is described in Section II-A1.

Once radiation is accurately calculated at a fine-resolution scale (i.e., solo slope), the corresponding variables at coarse-resolution scales (i.e., composite slope) can be generated using upscaling procedures. Currently, most relevant studies are focused on thermal regions. Several studies have used this upscaling method to estimate surface temperature [6], [7], [37], [39] and surface long-wave radiation [12], [13] for composite slopes. In short-wave bands, parameterization of solar radiation is often adopted in land surface models to accelerate calculations [11], [40]–[42] but with the sacrifice of accuracy. In addition, the concept of an equivalent slope model is proposed and applied to find the equivalent slope and aspect for composite slopes [19], [43], [44]. Wen *et al.* [14] converted fine-scale albedo to coarse-scale albedo in a rugged terrain using a simulated DEM. Wu *et al.* [36] defined surface reflectance quantities for rugged terrains from the perspective of bidirectional reflection distribution function, which provides bases for composite-slope modeling at short-wave bands.

In summary, there exist accurate models and algorithms to simulate RT processes over both solo and composite slopes. However, this simulation can be computationally expensive, as explained above, when using the accurate Proy algorithm to calculate terrain radiation over fine-resolution DEM. Therefore, various approximation methods are adopted to accelerate the calculation.

1) The calculation of terrain radiation is approximated since it is the most computationally expensive part. Using fewer iterations instead of waiting for the convergence point reduces the computation time. Besides, using the terrain view factor (TVF), which was proposed to approximate surrounding topographic conditions and radiation fluxes, not only avoids iterations but greatly reduces computations within the search radius. These two methods (fewer iterations and TVF method) are from the perspective of approximating terrain radiation.
2) The assumption of a solo slope for a coarse-scale pixel (composite slope) can be made, indicating that the spatial resolutions of the DEM and target parameter are identical. In addition, many studies do not consider topographic effects on coarse-resolution data at all, which means that the surface is assumed to be flat. These two methods (solo-slope and flat-surface assumptions) are from the perspective of reducing within-pixel calculations.

Details of the four approximation methods are further explained in Section II-B.

Finally, it is worth noticing that topographic and atmospheric effects are actually coupled, and correcting these combined effects is also an important topic. However, current study focuses on the influences of topography only; thus, all the models, simulations, and analyses are conducted at the surface level. Readers interested in the correction of combined atmospheric and topographic effects can refer to the references [3]–[5], [45]–[53].

This study aims to analyze the errors associated with the four topographic approximation methods in simulating various surface parameters at a series of spatial resolutions (i.e., solo and composite slopes). These surface parameters include surface reflectance, directional brightness temperature, surface radiation, absorbed photosynthetically active radiation (APAR), SIF, surface albedo, and surface emissivity. Surface models for these parameters over composite slopes were first proposed. Then, three typical land covers (vegetation, soil, and snow) were assumed and tested, and the wavelength ranged from the optical to thermal regions. The surface parameters were simulated and analyzed at different spatial scales (30, 90, 270, 540, 1080, and 5400 m) because the influences of topography on surface parameters can be very different at multiple spatial scales [54]–[56]. The surface models provided in this study can be used for estimating surface parameters over rugged terrains. Also, the analyses of topographic effects on various surface parameters provide advice on which method is appropriate (considering accuracy and computational time) when estimating a particular parameter.

II. Methodology

A. Terrain Models

The related terrain models at the surface level are first developed to calculate surface reflectance, directional brightness temperature, surface albedo, surface emissivity, APAR, SIF, and surface net radiation.

1) Solo-Slope Models: As reviewed in Section I, various solo-slope models are available for different parameters. However, such studies have focused on specific parameters; thus, the multiparameter modeling framework developed in [57] is adopted in this study. In [57], an optical-thermal RT model coupling framework that considered topographic effects was developed. This framework can simulate surface radiance/reflectance, surface downward/upward/net radiation, surface albedo/emissivity, and FAPAR/APAR over solo slopes. Evaluation of this framework using the 3-D ray-tracing DART model and field measurement demonstrates that it is highly accurate.

Three surface types (vegetation, soil, and snow) are tested in this study, of which the canopy RT model over terrains (4SAILT) [27], the SIF model over terrains (SIFT) [33], the Walthall soil model [58], and the asymptotic radiative transfer (ART) snow model [59] are used. The 4SAILT is an extension of the 4SAIL canopy RT model [60]; the SIFT is an RT model for SIF simulations, which is an extension of the well-known SCOPE-SIF model [61]. Both the 4SAILT and SIFT are designed for solo slopes, and they consider topographic effects on direct solar radiation, surrounding topography obstruction of hemispherical radiation, and gravitropic influences on the leaf angle distribution (LAD). The Walthall model is an empirical soil model that accounts for anisotropic surfaces, and a soil spectrum is needed to drive the model. The ART snow model simulates the optical properties of snow, and it utilizes two main parameters: the snow grains diameter and the pollutant proportion. The imaginary part of the ice refractive index is also needed in ART, and its values came from [62] in this study. The Walthall and ART models are adapted to be used for solo slopes using the topographic algorithm in [27]. Without a loss of generality, the leaf and soil spectra (0.35–15 μm) used in [27] were taken as input in this study.

In general, radiance observed by a sensor at the bottom of the atmosphere (BOA) from a solo slope can be expressed as follows:

$$L_o^{\text{solo}} = L^{\text{tge}} + L^{\text{adj}} = L^{\text{tge}} + r_{do}E^{\text{adj}}/\pi \tag{1}$$

where L^{tge} is the radiance from the target pixel only (without interaction with adjacent slopes)

$$L^{\text{tge}} = \frac{1}{\pi}[r_{so}F_{\text{sun}}E_{\text{dir}} + r_{do}V_{\text{sky}}(E_{\text{dif}} + E_{\text{atm}})] + \varepsilon_o B(T) \tag{2}$$

and L^{adj} is the radiance contributed by adjacent pixels. r_{so} and r_{do} are the bidirectional reflectance factor and hemispherical-directional reflectance factor of the target slope, respectively. ε_o is the directional emissivity in the viewing direction. E_{dir}, E_{dif}, and E_{atm} represent downward solar direct radiation, downward solar diffuse radiation, and downward atmospheric thermal radiation, respectively, at the BOA. B is Planck's function, and T is the temperature in Kelvin. F_{sun} is the transformation factor for direct radiation [27]

$$F_{\text{sun}} = \zeta \cos\theta_{is}/\cos\theta_s \tag{3}$$

where ζ is a binary factor (0 or 1) that indicates whether the pixel is self-shadowed or shielded by other pixels; $\cos\theta_s$ is the solar zenith angle referring to the horizontal plane; and $\cos\theta_{is}$ is the solar zenith angle referring to the slope surface. V_{sky} is the sky view factor (SVF), which can be calculated for isotropic radiation [63] as follows:

$$V_{\text{sky}} = \frac{1}{N}\sum_{i=1}^{N}\left[\cos\beta\sin^2 H_{\varphi_i} + \sin\beta\cos(\varphi_i - \varphi_T) \times (H_{\varphi_i} - \sin H_{\varphi_i}\cos H_{\varphi_i})\right] \tag{4}$$

where N is the number of discretized search directions; φ_i is the azimuth angle of direction i; and H_{φ_i} is the horizon angle in direction i. DEM data are needed to accurately calculate V_{sky}.

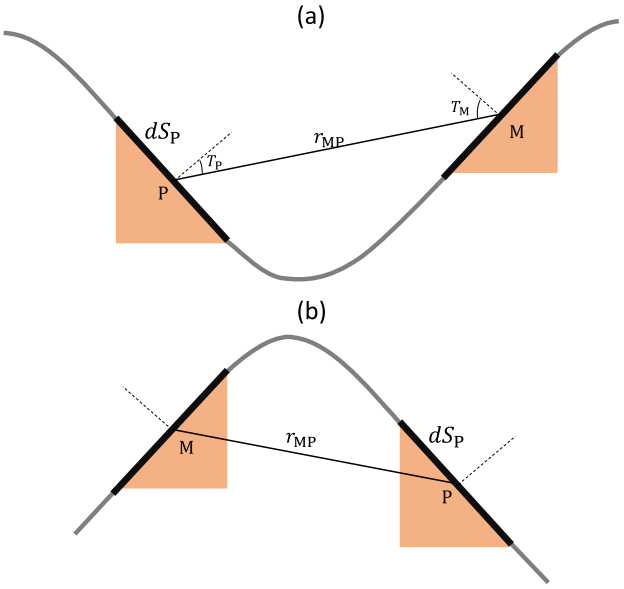

Fig. 1. Schematic for calculating terrain radiation using the Proy algorithm. M represents the slope associated with the target pixel, and P represents an adjacent slope. dS_{P} is the area of slope P; T_{M} and T_{P} are the angles of points M and P between the normal vector of the inclined surface and the line MP; and r_{MP} is the distance between M and P. (a) Example of the situation that P is visible to M. (b) Example of the situation that P is invisible to M.

E^{adj} is the irradiance from adjacent slopes (P), which is visible from the current slope (M) and is accurately calculated, as shown in Fig. 1, using the Proy algorithm [1]

$$E^{\text{adj}} = \sum_{i=1}^{N_s}\zeta_{\text{MP}}^{i}\frac{\cos T_{\text{M}}\cos T_{\text{P}}dS_{\text{P}}}{r_{\text{MP}}^2}L^{\text{adj}}(i) \tag{5}$$

where N_s is the number of surrounding pixels of M; ζ_{MP}^{i} (1 or 0) indicates whether P is visible to M or not; dS_{P} is the area of slope P; T_{M} and T_{P} are the angles of points M and P between the normal vector of the inclined surface and the line MP; r_{MP} is the distance between M and P; and L^{adj} is the reflected/emitted radiance of P. The search radius of 1 km is adopted in this study.

It should be noted that the Proy algorithm is a radiosity method. An iteration process is needed to calculate L_o^{solo} in (1) with the consideration of adjacent contributions. E^{adj} is set to 0 at the zero iteration (zero instead first is used here to indicate there are no adjacent contributions at now), and L_o^{solo} is calculated. At the first iteration, the calculated L_o^{solo} is served as L^{adj} in (5) to calculate E^{adj} for every pixel, and then,

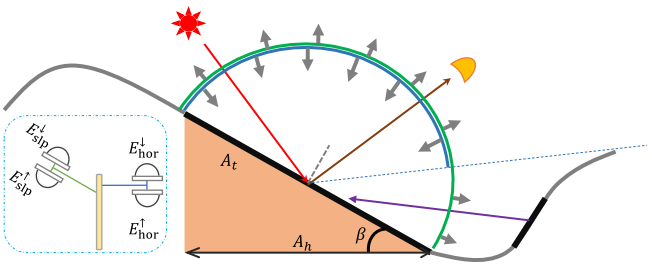

Fig. 2. Schematic of the topographic effects on sensor observations and surface radiation fluxes. The red arrow indicates sunrays, the brown arrow is the view direction, and the purple arrow represents terrain radiation from adjacent slopes. The blue arc represents the percentage of the visible sky from the target slope, while the green arc indicates the upper hemispherical space that refers to the slope surface. The horizontal and slope-parallel sensors measure radiation fluxes in reference to the horizontal plane and radiation fluxes in reference to the slope surface, respectively. A_h and A_t are the size of the pixel and slope surface, respectively. β is the slope value.

the calculated E^{adj} is input to (1) to update L_o^{solo}. The sensor radiance calculated at this point includes adjacent contributions (one-iteration result). At the second iteration, L_o^{solo} in the last iteration is input to (5) to update E^{adj}, which is then inputted to (1), the get new L_o^{solo} (two-iteration result). The iterations continue until the results of two iterations barely change (e.g., less than 0.1%). In this study, four iterations are good enough for all pixels over the study area (described in Section II-C) to achieve that. Also, as we can see, this iteration process can be computationally expensive for high-resolution DEM (e.g., the 30-m DEM used in this study) because there are hundreds of pixels within the 1-km search radius.

A schematic is used to illustrate the differences between radiation referring to the slope surface and radiation referring to the horizontal plane before performing the following steps. As shown in Fig. 2, the radiation received by the target slope includes the direct solar radiation (red arrow), diffuse sky radiation (downward gray arrows), and terrain radiation from adjacent slopes (purple arrow). Due to the obstruction of the surrounding topography, the solid angle of downward sky radiation is less than 2π (blue arc). In contrast, the upward reflected/emitted radiation distribution in the upper 2π hemisphere refers to the slope surface (green arc). If horizontal and slope-parallel sensors (as shown on the left side of Fig. 2) are placed in the slope, the measured downward (upward) radiation that refers to the slope surface would be different from the measured downward (upward) radiation that refers to the horizontal plane. Detailed modeling of these parameters can be found in [57].

Therefore, the downward radiation on the solo slope ($E_{d\_\text{slp}}^{\text{solo}}$), the upward radiation from the solo slope ($E_{u\_\text{slp}}^{\text{solo}}$), the radiation absorbed by vegetation that referred to the slope (E_a^{solo}), the downward radiation on the horizontal plane ($E_{d\_\text{hor}}^{\text{solo}}$), and the upward radiation from the horizontal plane ($E_{u\_\text{hor}}^{\text{solo}}$) can be expressed as follows:

$$E_{d\_\text{slp}}^{\text{solo}} = E_{d\_\text{slp}}^{\text{tge}} + E_{d\_\text{slp}}^{\text{adj}} = E_{d\_\text{slp}}^{\text{tge}} + E^{\text{adj}} \tag{6a}$$

$$E_{u\_\text{slp}}^{\text{solo}} = E_{u\_\text{slp}}^{\text{tge}} + E_{u\_\text{slp}}^{\text{adj}} = E_{u\_\text{slp}}^{\text{tge}} + r_{dd}E^{\text{adj}} \tag{6b}$$

$$E_a^{\text{solo}} = E_a^{\text{tge}} + E_a^{\text{adj}} = E_a^{\text{tge}} + \alpha_d E^{\text{adj}} \tag{6c}$$

$$E_{d\_\text{hor}}^{\text{solo}} = E_{d\_\text{hor}}^{\text{tge}} + E_{d\_\text{hor}}^{\text{adj}} = E_{d\_\text{hor}}^{\text{tge}} + V_{\text{sky}}E^{\text{adj}} \tag{6d}$$

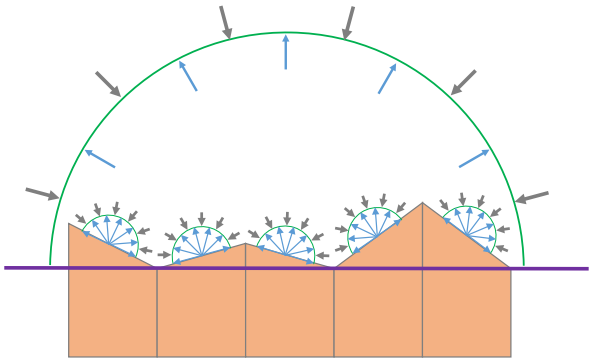

Fig. 3. Schematic of upward and downward radiation fluxes for a composite slope. This composite slope contains five solo slopes. The gray and blue arrows indicate downward and upward radiation fluxes, respectively. The solid purple line indicates the horizontal plane, and the green arc represents the 2π hemisphere. Horizontal downward and upward radiation fluxes of the composite slope are illustrated by the large green arc. Slope downward (upward) radiation fluxes are the sum of downward (upward) radiation fluxes on (from) the five solo slopes.

$$E_{u\_\text{hor}}^{\text{solo}} = E_{u\_\text{hor}}^{\text{tge}} + E_{u\_\text{hor}}^{\text{adj}} = E_{u\_\text{hor}}^{\text{tge}} + V_{\text{sky}}r_{dd}E^{\text{adj}} \tag{6e}$$

where

$$E_{d\_\text{slp}}^{\text{tge}} = F_{\text{sun}}E_{\text{dir}} + V_{\text{sky}}(E_{\text{dif}} + E_{\text{atm}}) \tag{7a}$$

$$E_{u\_\text{slp}}^{\text{tge}} = r_{sd}F_{\text{sun}}E_{\text{dir}} + r_{dd}V_{\text{sky}}(E_{\text{dif}} + E_{\text{atm}}) + \pi\varepsilon_d B(T) \tag{7b}$$

$$E_a^{\text{tge}} = \alpha_s F_{\text{sun}}E_{\text{dir}} + \alpha_d V_{\text{sky}}(E_{\text{dif}} + E_{\text{atm}}) \tag{7c}$$

$$E_{d\_\text{hor}}^{\text{tge}} = \zeta E_{\text{dir}} + V_{\text{sky}}(E_{\text{dif}} + E_{\text{atm}}) \tag{7d}$$

$$E_{u\_\text{hor}}^{\text{tge}} = V_{\text{sky}}E_{u\_\text{slp}}^{\text{tge}} \tag{7e}$$

and r_{sd} and r_{dd} are the directional-hemispherical reflectance and the bihemispherical reflectance, respectively. ε_d is the hemispherical emissivity of the surface. α_s and α_d are the absorptances of vegetation for direct and diffuse radiation [64], [65], respectively, and they both equal 0 for nonvegetated pixels. The contribution of E_{atm} in (7c) can be neglected at the visible spectrum range.

Similar to L_o^{solo}, calculations of $E_{d\_\text{slp}}^{\text{solo}}$, $E_{u\_\text{slp}}^{\text{solo}}$, E_a^{solo}, $E_{d\_\text{hor}}^{\text{solo}}$, and $E_{u\_\text{hor}}^{\text{solo}}$ also require iteration processes, and the steps are the same as the calculation of L_o^{solo}. Also, four iterations are adopted for calculating these radiation parameters over the study area (as described in Section II-C).

At this point, the fine-scale surface parameters are calculated with the consideration of adjacent contributions using the Proy algorithm.

2) Composite-Slope Models: Sensor radiance and surface radiation at coarse spatial resolution scales (i.e., composite slope) can be generated once the corresponding values have been calculated at a fine spatial resolution (i.e., solo slope). However, radiation on slopes and the horizontal plane still need to be discriminated against that over composite slopes. As shown in Fig. 3, the downward and upward radiation fluxes that refer to the horizontal plane (purple line) for the composite slope are illustrated by the large green arc and are labeled horizontal downward and upward radiations in this study. In contrast, the sum of downward (upward) radiation fluxes on (from) the solo slopes, which is labeled as slope downward (upward) radiation, is different from the horizontal downward (upward) radiation. Slope and horizontal

parameters may play different roles according to practical applications. For example, slope absorbed radiation is needed when exploring the amount of solar radiation absorbed by vegetation, while horizontal radiation is needed when studying the surface energy balance.

The equations used to calculate sensor radiance, slope radiation, and horizontal radiation of a composite slope are given as follows:

$$L^{\text{comp}} = \frac{\sum_{p=0}^{N_f} L^{\text{solo}} \cos\theta_{iv}^p \zeta^p dA_t^p}{\sum_{p=0}^{N} \cos\theta_{iv}^p \zeta^p dA_t^p} \tag{8}$$

$$E_{\text{slp}}^{\text{comp}} = \frac{\sum_{p=0}^{N_f} E_{\text{slp}}^{\text{solo}} dA_t^p}{\sum_{p=0}^{N} dA_t^p} \tag{9}$$

$$E_{\text{hor}}^{\text{comp}} = \frac{\sum_{p=0}^{N_f} E_{\text{hor}}^{\text{solo}} dA_h^p}{\sum_{p=0}^{N} dA_h^p} \tag{10}$$

where N_f is the number of fine-scale pixels (solo slopes) within one coarse-scale pixel (composite slope); $\cos\theta_{iv}^p$ is the view zenith angle referring to the slope surface; ζ^p is a binary factor that indicates whether the current fine-scale pixel can be observed ($\zeta^p = 1$) or not ($\zeta^p = 0$); dA_h^p is the area of pixel p, while dA_t^p is the area of the corresponding sloping surface; and $dA_h^p = dA_t^p \cos\beta^p$, where β^p is the slope value of pixel p.

Similarly, the total emitted SIF by all leaves (F_e) that refers to the slope surface and the SIF observed at the top of the canopy (F_o) are calculated as follows:

$$F_e = \frac{\sum_{p=0}^{N_f} F_{\text{slp}}^{\text{solo}} dA_t^p}{\sum_{p=0}^{N} dA_t^p} \tag{11}$$

$$F_o = \frac{\sum_{p=0}^{N_f} F_o^{\text{solo}} \cos\theta_{iv}^p \zeta^p dA_t^p}{\sum_{p=0}^{N} \cos\theta_{iv}^p \zeta^p dA_t^p} \tag{12}$$

where $F_{\text{slp}}^{\text{solo}}$ and F_o^{solo} are the total emitted SIF referring to the slope surface and the observed SIF for a solo slope, respectively. $F_{\text{slp}}^{\text{solo}}$ and F_o^{solo} are derived from the actual solar radiation received by a solo slope, i.e., $E_{d\_\text{slp}}^{\text{solo}}$, and the detail modeling process can be found in [33].

The surface net radiation of a composite slope (E_n) can be calculated by the following formula:

$$E_n = \int_{\lambda_1}^{\lambda_2} \left[E_{d\_\text{hor}}^{\text{comp}}(\lambda) - E_{u\_\text{hor}}^{\text{comp}}(\lambda)\right] d\lambda \tag{13}$$

where $E_{d\_\text{hor}}^{\text{comp}}$ and $E_{u\_\text{hor}}^{\text{comp}}$ represent the downward and upward radiations, respectively. λ is the wavelength, and λ_1 and λ_2 are the upper and lower bounds of integration, respectively. The slope downward radiation fluxes (E_d) and slope APAR are calculated as follows:

$$E_d = \int_{\lambda_1}^{\lambda_2} E_{d\_\text{slp}}^{\text{comp}}(\lambda) d\lambda \tag{14}$$

$$\text{APAR} = \int_{\lambda_1}^{\lambda_2} E_{a\_\text{slp}}^{\text{comp}}(\lambda) d\lambda \tag{15}$$

where $E_{d\_\text{slp}}^{\text{comp}}$ and $E_{a\_\text{slp}}^{\text{comp}}$ represent the downward and absorbed radiation fluxes that refer to the slope surface, respectively. λ_1 and λ_2 are 0.4 and 0.7 μm, respectively, for APAR.

The surface broadband albedo (α) can be calculated by (16) if thermal emissions are neglected, while the surface broadband hemispherical emissivity (ε) can be calculated by (17) if neglecting solar radiation

$$\alpha = \frac{\int_{\lambda_1}^{\lambda_2} E_{u\_\text{hor}}^{\text{comp}}(\lambda) d\lambda}{\int_{\lambda_1}^{\lambda_2} E_{d\_\text{hor}}^{\text{comp}}(\lambda) d\lambda} \tag{16}$$

$$\varepsilon = \frac{\int_{\lambda_1}^{\lambda_2} E_{u\_\text{hor}}^{\text{comp}}(\lambda) d\lambda}{\pi \int_{\lambda_1}^{\lambda_2} B(\lambda, T) d\lambda}. \tag{17}$$

Correspondingly, the surface reflectance (ρ) and directional brightness temperature (T_b) are calculated as follows:

$$\rho = \pi L^{\text{comp}} / E_{\text{BOA}} \tag{18}$$

$$T_b = B^{-1}(L^{\text{comp}}) - 273.15 \tag{19}$$

where E_{BOA} is the total downward radiation at the BOA; B^{-1} is the inverse form of Planck's function; and T_b is quantified in Celsius degree in this study.

B. Approximation Methods

As described in Section II-A, the calculations of terrain radiation using the Proy algorithm (i.e., the solo-slope and composite-slope models presented above) are accurate but can be computationally expensive for fine-scale DEM (e.g., the 30- and 90-m DEM used in this study). Hence, four different approximation methods are often used to accelerate the computation process.

1) Fewer Iterations: As described in Section II-A1, the accurate calculation requires iterative processing until a particular criterion is achieved. However, this is the most time-consuming step during a simulation. As summarized in Section I, many studies do not conduct the iteration process, which means that E_{adj} is set to 0 since the iteration process is used for calculating adjacent contributions. As a compromise between efficiency and accuracy, performing fewer iterations (like only once) seems like a good option, but which number of iterations is appropriate still lacks evaluation.

2) TVF Method: Instead of neglecting terrain irradiance, the approximation method used to simulate adjacent contributions implements the TVF [2], [63], which is calculated as follows:

$$V_{\text{terr}} = \frac{1 + \cos\beta^p}{2} - V_{\text{sky}} \tag{20}$$

and the adjacent contributions are approximated by

$$E^{\text{adj}} = \pi V_{\text{terr}} \overline{L}^{\text{adj}} \tag{21}$$

where $\overline{L}^{\text{adj}}$ is the average of radiance reflected/emitted from surrounding slopes.

It should be noted that the TVF method is used to approximate the adjacent contributions only, and a fine-resolution DEM is still required.

3) Solo-Slope Assumption: For composite-slope modeling, the solo-slope assumption can be used to avoid looping over fine-scale DEM pixels, which means that the spatial resolution of the DEM used is the same as the target parameter.

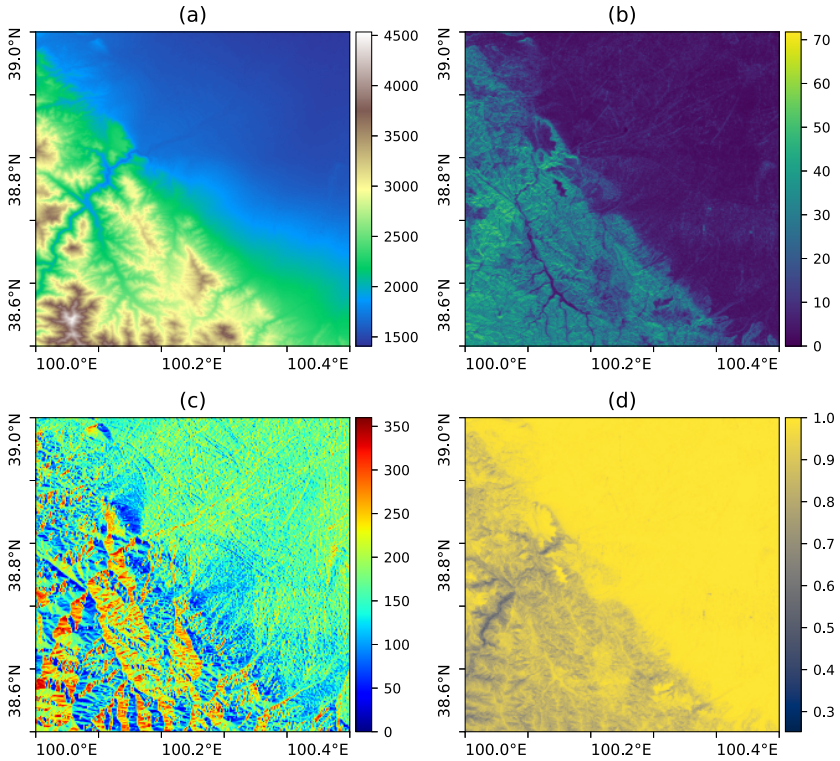

Fig. 4. Terrain parameters of the study area. (a) Elevation in meter. (b) Slope in degree. (c) Aspect in degree. (d) SVF.

4) Flat-Surface Assumption: The assumption of flat-surface pixels, meaning that topography is not considered at all, is also an option. This assumption has been widely adopted in the retrieval of surface parameters from coarse spatial resolution data.

C. Study Area and Data

The study area (38.5°N–39.0°N, 100.0°E–100.5°E) is located at the northeastern edge of the Tibetan Plateau. As shown in Fig. 4, it was chosen because mountains and plains occupy approximately 50% of the area; it contains terrains in various conditions (from gentle slopes to steep slopes). Therefore, the influences of topography can be demonstrated in a contrastive way.

The ASTER Global Digital Elevation Model (ASTGTM) global 1-arc-second dataset [66] is used, and it is further used to calculate the slope, aspect, and SVF [63], [67], [68]. The spatial resolution of ASTGTM is approximately 30 m; this spatial resolution is taken as the finest resolution (solo slope) in this study. The DEM data are then resampled to 90, 270, 540, 1080, and 5400 m, respectively. These five spatial resolutions are used for composite-slope simulations in this study.

It should be noted that this study only uses the DEM of this area. The actual surface conditions (e.g., land cover and vegetation growth) are not used. A detailed experimental scheme is described in Section II-D.

D. Experimental Scheme

A simulation-based experimental scheme is designed in this study. Three surface types (vegetation, soil, and snow) are assumed. Then, three independent simulation tasks are conducted, which assumes that all of the study areas are covered by vegetation, soil, and snow, respectively. In this way, we can get more comprehensive datasets than using actual surface conditions. This strategy is usually adopted to diagnose the influences of interested variables (i.e., topography in this study).

The errors of the topographic approximation methods presented in Section II-B are analyzed using multiple simulated parameters at a series of spatial resolutions (30, 90, 270, 540, 1080, and 5400 m). These parameters include surface reflectance (ρ) and/or directional brightness temperature (T_b) at the center wavelength of Landsat-8 channels (0.44, 0.48, 0.56, 0.65, 0.87, 1.61, 2.2, 11.1, and 12.0 μm), slope downward radiation (E_d), surface net radiation (E_n), slope APAR, observed (F_o) and total emitted (F_e) SIF at 760 nm, surface broadband albedo (α), and surface broadband hemispherical emissivity (ε). These approximation methods are tested over the three surface types mentioned above.

Parameters for each surface type and observational geometry are fixed, and BOA irradiance is also fixed. The terrain parameters of the study area are used. Therefore, differences in the data images are caused only by topography. The solar zenith angle and the solar azimuth angle are 30° and 150°, respectively, and the sensor is nadir-viewed. A leaf area index of 3 and a spherical LAD are assumed for the vegetated-surface simulation, and a leaf and soil spectrum covering 0.35–15 μm in [27] is used for 4SAILT. A leaf chlorophyll content of 60 μg/cm^2 is used for SIF simulations, and the fluorescence quantum efficiencies of photosystems I and II are 0.002 and 0.01, respectively. This soil spectrum is also used as the input for the Walthall soil model in the soil-surface simulation. The snow grains diameter, which is used for the

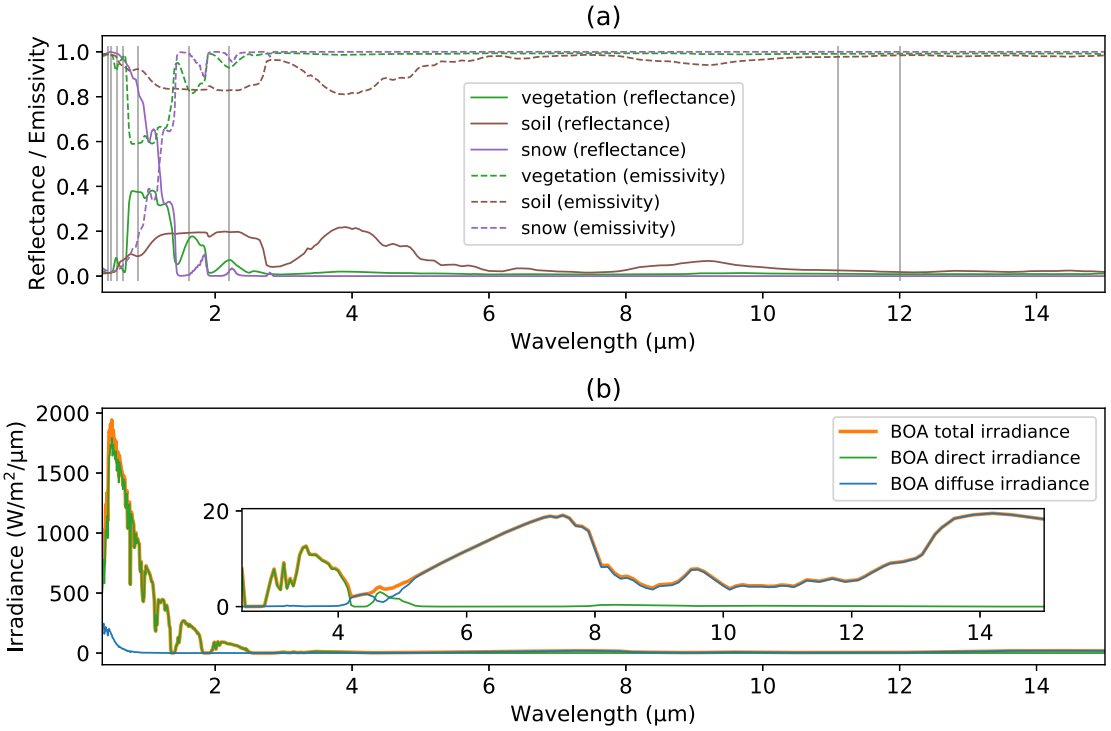

Fig. 5. (a) Bidirectional reflectance factor and directional emissivity spectra of vegetation, soil, and snow. Solar zenith angle is 30°, the solar azimuth angle is 150°, nadir-viewing, and the slope is 0. The gray vertical lines represent the center wavelength of Landsat-8 channels. (b) Downwelling irradiance spectra at the BOA used in this study.

ART model, is assumed to be 400 μm for the snow-surface simulation. The surface temperature is set to 20 °C and 25 °C for the vegetation and soil simulations, respectively, while it is set to 0 °C for the snow simulation. As an illustration, the reflectance and directional emissivity spectra simulated by the three models (4SAILT, Walthall, and ART) over a flat surface are shown in Fig. 5(a). The center wavelengths of the Landsat-8 channels are also plotted. Fig. 5(b) shows the BOA irradiance used in simulations. The detailed parameter settings of these four RT models (4SAILT, Walthall, ART, and SIFT) are given in Table I.

III. Results and Analyses

A. Topographic Effects on Surface Reflectance and Directional Brightness Temperature

As an illustration and example, the simulated surface reflectances (0.87 μm; i.e., ρ_5) of the vegetated surface at a series of spatial resolutions (30, 90, 270, 540, 1080, and 5400 m) are shown in Fig. 6. Each row of Fig. 6 includes data representing a specific resolution. The subplots with the title "solo" represent data that are simulated with the solo-slope assumption, and the subplots with the title "tvf" indicate that the TVF method is used. "Lj" ($j = 1, 2, 3, 4$) indicates the use of the iteration method, and j is the number of iterations. Specifically, the L0 images do not consider adjacent contributions, i.e., terrain radiation. As j increases, the simulation results become more accurate. Therefore, the L4 images have the highest accuracy and are taken as the benchmark for further evaluation. The L2 and L3 images are not plotted because they do not show notable differences from L4 in Fig. 6. In addition, images made with the assumption of flat surfaces only contain one value since all parameters are fixed except topography; thus, they are also not plotted. Errors induced by different topographic assumptions are shown in Fig. 7, in which the L4 images are taken as references. Discrepancies between the images with various assumptions (flat surface, solo slope, TVF, and fewer iterations) and the reference images are shown in different columns, where the absolute values of the corresponding errors are plotted.

The surface reflectance at 0.87 μm over the flat vegetated surface is 0.376, and topography changes it obviously, as shown in Fig. 6. It can be seen from Figs. 6 and 7 that: 1) details in the images are lost with decreasing of spatial resolution; 2) topography does not exert significant influences over the plane areas (upper triangle part), where the SVF values are large and the slope values are small; 3) both the flat-surface and solo-slope assumptions induce significant errors over mountain areas for all spatial resolutions; 4) terrain radiation cannot be ignored for small-SVF areas when using high spatial resolution data; 5) the TVF method does not perform well in simulating adjacent contributions, and it may introduce additional uncertainties; and 6) one iteration is sufficient when considering adjacent contributions over the vegetated surface, and more iterations do not add considerable value.

In order to avoid repetitive descriptions, statistical tables contain the mean percentage error (MPE) over the mountains of the study area (lower triangle part) for each surface parameter are used, and the threshold of 0.1% is taken as a criterion.

The statistics of MPE for ρ and T_b over vegetation, soil, and snow coverages are given in Table II. Numbers in blue indicate that the corresponding approximation method is acceptable (MPE $<= 0.1\%$), while the red color represents the

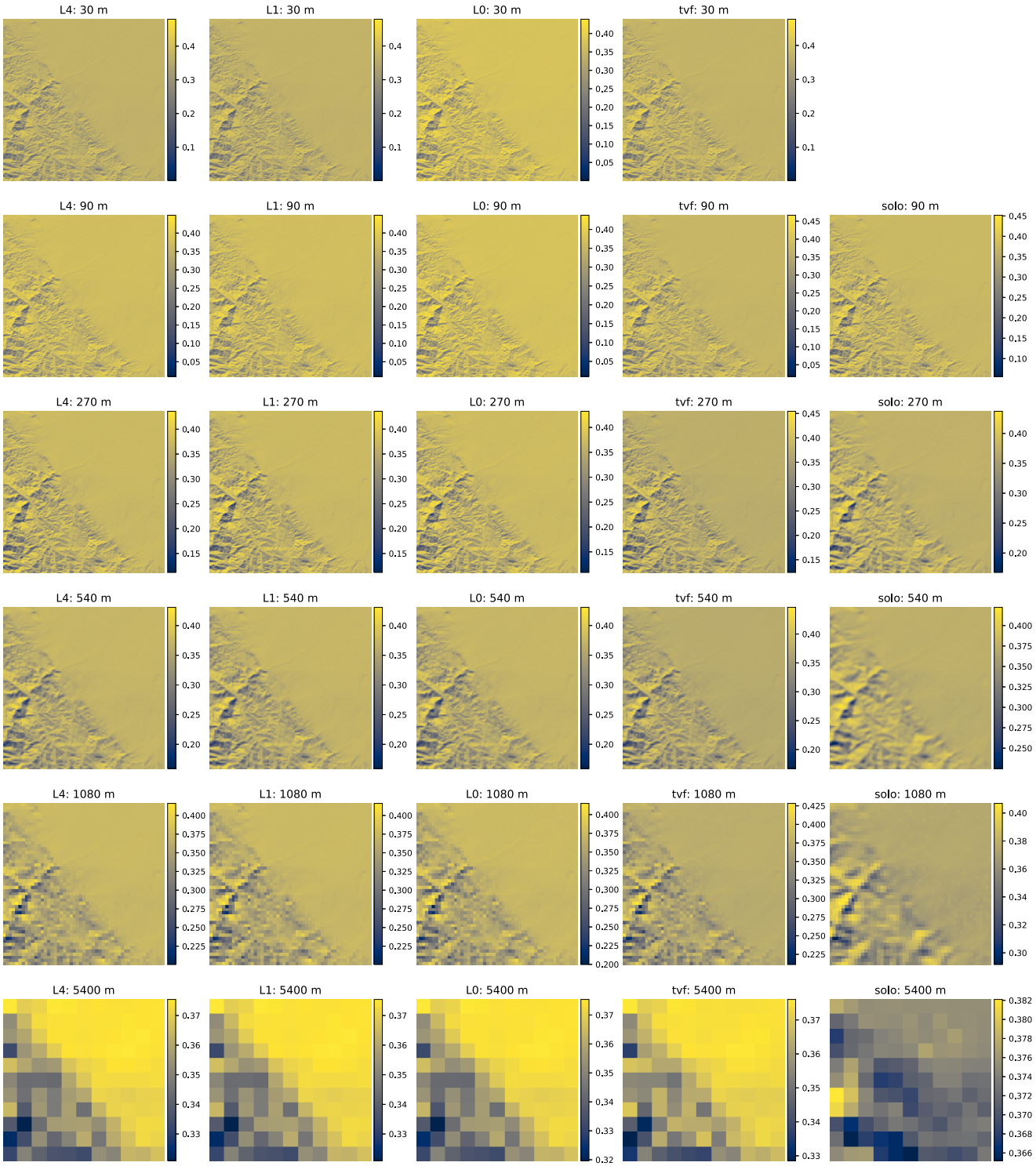

Fig. 6. Simulated surface reflectance (0.87 μm) for the vegetated surface. Each row includes data at a specific resolution (30, 90, 270, 540, 1080, and 5400 m). "solo" represents data simulated with the assumption of a solo slope, and "tvf" represents results with the TVF used. "Lj" ($j = 1, 2, 3, 4$) indicates the fine-resolution DEM method, where topography within one pixel is considered, and j is the number of iterations. As j increases, the simulation results become more accurate. Therefore, the L4 images are used as the benchmark. Images for L2 and L3 are not shown.

accuracy of the corresponding method is beyond the threshold (MPE $>$ 0.1%). Table II demonstrates that both the solo-slope and flat-surface assumptions induce significant errors (1%–58%) in ρ_1–ρ_7. It also shows that topography has more influences on highly reflective areas/bands (e.g., ρ_5 for vegetation and ρ_1–ρ_4 for snow) than on areas/bands with a low reflectively (e.g., ρ_1 for vegetation). Similarly, adjacent contributions are more important in highly reflective areas/bands than in areas/bands with low reflectivity. For example, ignoring adjacent contributions has little effect on soil and vegetation simulations in low-reflective bands (L0 numbers for ρ_1–ρ_4 in the Vegetation and Soil columns are all blue), while adjacent contributions are significant for snow simulations (L0 numbers for ρ_1–ρ_4 in the Snow column

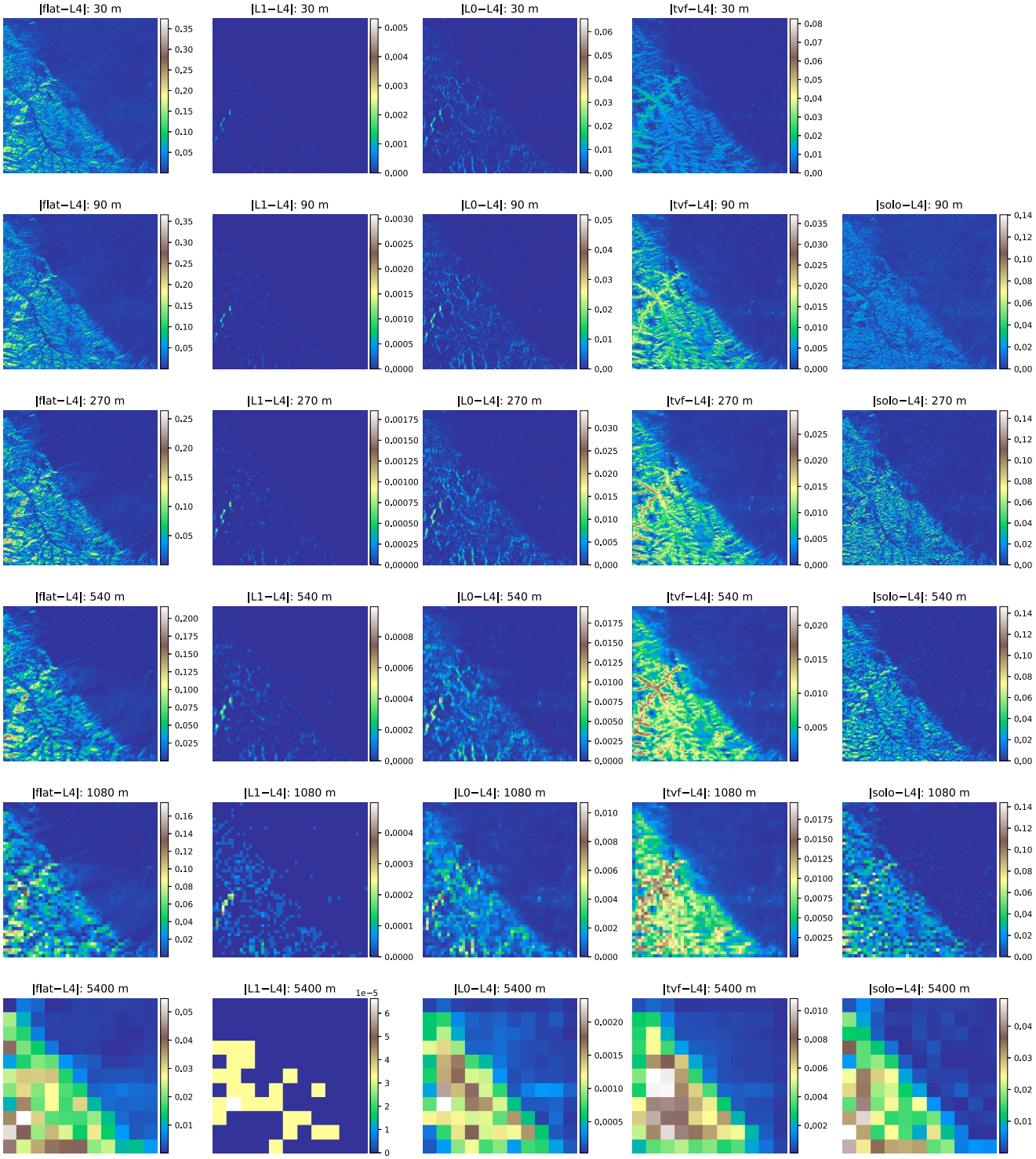

Fig. 7. Discrepancies between the simulated surface reflectance (0.87 μm) and the benchmark (L4 image) for the vegetated surface. Each row includes data at a specific resolution (30, 90, 270, 540, 1080, and 5400 m). "|flat–L4|" represents errors induced by ignoring topography, "|solo–L4|" represents errors induced by the assumption of a solo slope, and "|tvf–L4|" represents errors induced by using the TVF. "|Lj–L4|" (j = 1, 2, 3) indicates errors by using fewer iterations. Images for "|L2–L4|" and "|L3–L4|" are not shown.

are red). In contrast, adjacent contributions are significant for the estimation of brightness temperature unless the surface is a blackbody. The reason is that a high emissivity means that the surface is closer to a blackbody than low emissivity areas and, thus, is less influenced by geometric angles.

The statistics of maximum error (MME) for ρ and T_b over vegetation, soil, and snow coverages are given in Table S1 in the supplemental file. Table S1 provides the same findings as in Table II. As an example, the directional emissivity value of snow at band 8 is 1.0, and it can be seen from both Tables II and S1 that the corresponding B_T^8 are barely

TABLE I
PARAMETER SETTING OF THE RT MODELS FOR THE EXPERIMENTAL SCHEME (FQE = FLUORESCENCE QUANTUM EFFICIENCY)

Model	Parameter	Values	Units
-	Solar zenith angle	30	degrees
	Solar azimuth angle	150	degrees
	View zenith angle	0	degrees
	View azimuth angle	90	degrees
	Slope	from DEM	degrees
	Aspect	from DEM	degrees
	Sky view factor	from DEM	-
	BOA irradiance	see Fig. 5(b)	-
4SAILT	Leaf area index	3	m^2/m^2
	Leaf and soil spectra	from [27]	-
	Leaf angle distribution	spherical	-
	Hotspot parameter	0	-
	Leaf temperature	20	°C
	Soil temperature	25	°C
Walthall	Soil spectrum	from [27]	-
	Soil temperature	25	°C
ART	Snow grain diameter	400	μm
	Pollutants proportion	0	-
	Snow temperature	0	°C
SIFT	Leaf area index	3	m^2/m^2
	Leaf angle distribution	spherical	-
	Hotspot parameter	0	-
	Leaf chlorophyll content	60	$\mu g/cm^2$
	Leaf carotenoids content	10	$\mu g/cm^2$
	Leaf water content	0.012	cm
	Leaf dry matter content	0.01	g/cm^2
	Leaf anthocyanins content	0	$\mu g/cm^2$
	Leaf structure parameter	1.8	-
	FQE of photosystem I	0.002	-
	FQE of photosystem II	0.01	-
	Soil spectrum	from [27]	-

affected by topography; while the directional emissivity values of the vegetated and soil surfaces are 0.992 and 0.978, respectively, and neglecting adjacent contributions can induce errors exceeded 0.1 °C.

B. Topographic Effects on Surface Net Radiation, Slope Downward Radiation, and APAR

The statistics of MPE in different topographic approximation methods on surface net radiation E_n (0.35–15 μm), slope downward radiation E_d (0.35–15 μm), and APAR (0.4–0.7 μm) are summarized in Table III. It can be seen that ignoring topography (flat-surface assumption) induces an error of approximately 3%–44% in surface net radiation, an error of 15%–28% in slope downward radiation, and 17%–26% in APAR. Errors induced by the solo-slope assumption increase with decreasing of pixel size because the topographic information is gradually lost with decreasing of spatial resolution. These findings tell us that both the flat-surface and solo-slope assumptions are inaccurate, which means that a fine-resolution DEM is required to estimate surface radiation fluxes accurately. Otherwise, significant errors would be induced even for coarse spatial resolution data. For example, ignoring topography for data obtained at a 5400-m resolution can cause an error of 17% in APAR. The TVF method does not perform well in estimating radiation fluxes, and its error is larger than the error produced by the L0 images (L0 does not consider adjacent contributions at all).

The statistics of MME for E_n, E_d, and APAR are given in Table S2 in the supplemental file, which provides similar conclusions. However, it should be noticed that Table III shows that one iteration is sufficient for adjacent contributions, which is the averaged results over the mountains. In contrast, as demonstrated in Table S2 (i.e., MME), one iteration is not good enough for estimating fine-resolution (30–270 m) E_d over snow surface in the worst case scenarios.

C. Topographic Effects on Surface Albedo and Emissivity

The influences of different topographic approximation methods on surface broadband albedo (α) and broadband hemispherical emissivity (ε) are shown in Table III. It can be seen from Table III that the flat-surface assumption induces errors of approximately 23%–44% in the surface albedo estimate, while the solo-slope assumption induces errors of approximately 6%–24%. These results demonstrate that both the flat-surface and solo-slope assumptions are not accurate regardless of the spatial resolution of the data images. Errors induced by the TVF method are larger than the L0 method, which means that the TVF method is not a good choice for albedo estimation. It can also be seen that adjacent contributions should be considered for accurately estimating surface albedo unless surface reflectivity is low (like the soil spectrum used in this study). Nevertheless, one iteration is sufficiently accurate. The statistical results show little difference over different surface types for emissivity. Table III shows that the flat-surface assumption induces an error of approximately 13% in emissivity, and the solo-slope assumption introduces errors of approximately 3%–12%. The error of the TVF method is larger than the L0 method, and the adjacent contributions are not significant for emissivity (L0 numbers are all blue). Therefore, the L0 method is the best choice for estimating emissivity.

D. Topographic Effects on Observed and Total Emitted SIF

The statistics of MPE in different topographic approximation methods on observed SIF (F_o, 760 nm) and total emitted (F_e, 760 nm) are summarized in Table IV, and the corresponding statistics of MME are summarized in Table S3 in the supplemental file. It can be seen that the flat-surface assumption induces an averaged error of approximately 5%–15% in F_o over the mountains of the study area. The errors in F_e induced by the flat-surface assumption are approximately 17%–27%. The solo-slope assumption also causes significant errors in both the F_o and F_e, as shown in Tables IV and S3. These results demonstrated that both the flat-surface and the solo-slope assumptions are inaccurate for SIF simulations over rugged areas. The TVF method also does not perform well in the simulations of F_o and F_e, with errors larger than that produced by the L0 method. Generally, the L0 images are accurate enough for spatial resolutions from 30 to 5400 m, which means that adjacent contributions are not essential for SIF simulations. The reason is that adjacent contributions are small at the visible spectrum range absorbed by vegetation to emit fluorescence.

TABLE II

MEAN PERCENTAGE ERRORS (MPE, IN%) IN SURFACE REFLECTANCE (ρ_1–ρ_7; BANDS 1–7 OF LANDSAT-8; 0.44, 0.48, 0.56, 0.65, 0.87, 1.61, AND 2.2 μm) AND DIRECTIONAL BRIGHTNESS TEMPERATURE (B_T^8 AND B_T^9; BANDS 8 AND 9 OF LANDSAT-8; 11.1 AND 12.0 μm) OVER THE MOUNTAINS OF THE STUDY AREA (LOWER TRIANGLE PART). RES IS SPATIAL RESOLUTION IN METER. A NUMBER IN BLUE INDICATE THAT THE CORRESPONDING APPROXIMATION METHOD IS ACCEPTABLE (MPE <= 0.1%), WHILE THE RED COLOR REPRESENTS ACCURACY OF THE CORRESPONDING METHOD IS BEYOND THE THRESHOLD (MPE > 0.1%)

	Res	Vegetation						Soil						Snow					
		L2	L1	L0	tvf	solo	flat	L2	L1	L0	tvf	solo	flat	L2	L1	L0	tvf	solo	flat
ρ_1	30	0.00	0.00	0.01	0.05	–	9.79	0.00	0.00	0.01	0.05	–	21.29	0.00	0.02	0.74	4.19	–	31.97
	90	0.00	0.00	0.01	0.05	2.69	8.98	0.00	0.00	0.01	0.04	4.28	19.37	0.00	0.02	0.73	4.03	6.57	28.62
	270	0.00	0.00	0.01	0.05	3.59	7.03	0.00	0.00	0.01	0.04	6.82	15.72	0.00	0.01	0.72	3.86	10.89	22.48
	540	0.00	0.00	0.01	0.04	3.06	5.24	0.00	0.00	0.01	0.04	7.35	13.43	0.00	0.01	0.70	3.75	12.28	18.92
	1080	0.00	0.00	0.01	0.04	2.54	3.73	0.00	0.00	0.01	0.04	8.09	12.06	0.00	0.01	0.68	3.64	13.85	16.92
	5400	0.00	0.00	0.00	0.04	1.32	1.25	0.00	0.00	0.00	0.02	8.59	10.61	0.00	0.01	0.54	2.92	14.56	14.65
ρ_2	30	0.00	0.00	0.01	0.05	–	10.26	0.00	0.00	0.01	0.05	–	22.35	0.00	0.02	0.74	4.21	–	34.39
	90	0.00	0.00	0.01	0.05	2.79	9.31	0.00	0.00	0.01	0.05	4.43	20.12	0.00	0.02	0.74	4.04	6.81	30.57
	270	0.00	0.00	0.01	0.05	3.72	7.27	0.00	0.00	0.01	0.05	6.96	16.16	0.00	0.01	0.71	3.85	11.17	23.88
	540	0.00	0.00	0.01	0.05	3.18	5.41	0.00	0.00	0.01	0.05	7.40	13.67	0.00	0.01	0.70	3.74	12.45	20.08
	1080	0.00	0.00	0.01	0.05	2.65	3.85	0.00	0.00	0.01	0.05	8.09	12.16	0.00	0.01	0.67	3.62	13.98	17.97
	5400	0.00	0.00	0.01	0.05	1.43	1.31	0.00	0.00	0.01	0.03	8.53	10.61	0.00	0.01	0.54	2.91	14.63	15.60
ρ_3	30	0.00	0.00	0.07	0.40	–	10.87	0.00	0.00	0.02	0.10	–	23.81	0.00	0.02	0.74	4.21	–	37.44
	90	0.00	0.00	0.07	0.39	2.90	9.62	0.00	0.00	0.02	0.09	4.60	20.96	0.00	0.01	0.73	4.01	7.05	32.82
	270	0.00	0.00	0.07	0.38	3.83	7.44	0.00	0.00	0.02	0.09	7.12	16.64	0.00	0.01	0.71	3.81	11.41	25.54
	540	0.00	0.00	0.07	0.37	3.22	5.50	0.00	0.00	0.02	0.09	7.46	13.93	0.00	0.01	0.69	3.69	12.57	21.50
	1080	0.00	0.00	0.07	0.36	2.58	3.88	0.00	0.00	0.02	0.09	8.08	12.26	0.00	0.01	0.67	3.57	14.04	19.31
	5400	0.00	0.00	0.05	0.29	1.20	1.21	0.00	0.00	0.01	0.07	8.48	10.60	0.00	0.01	0.53	2.87	14.62	16.83
ρ_4	30	0.00	0.00	0.02	0.11	–	14.06	0.00	0.00	0.04	0.24	–	25.13	0.00	0.01	0.73	4.18	–	38.99
	90	0.00	0.00	0.02	0.10	3.26	12.02	0.00	0.00	0.04	0.23	4.69	21.40	0.00	0.01	0.72	3.94	7.12	33.48
	270	0.00	0.00	0.02	0.10	4.25	9.23	0.00	0.00	0.04	0.22	7.20	16.88	0.00	0.01	0.69	3.73	11.44	25.89
	540	0.00	0.00	0.02	0.10	3.49	6.86	0.00	0.00	0.04	0.22	7.48	14.04	0.00	0.01	0.68	3.61	12.51	21.70
	1080	0.00	0.00	0.02	0.09	2.75	4.93	0.00	0.00	0.04	0.21	8.07	12.29	0.00	0.01	0.65	3.50	13.92	19.44
	5400	0.00	0.00	0.01	0.08	1.12	1.72	0.00	0.00	0.03	0.17	8.43	10.56	0.00	0.01	0.52	2.81	14.45	16.91
ρ_5	30	0.00	0.00	0.35	2.08	–	19.13	0.00	0.00	0.05	0.32	–	29.06	0.00	0.01	0.66	3.86	–	39.31
	90	0.00	0.00	0.35	1.92	3.69	14.25	0.00	0.00	0.05	0.29	4.76	21.78	0.00	0.01	0.64	3.53	6.78	31.51
	270	0.00	0.00	0.34	1.87	5.29	11.08	0.00	0.00	0.05	0.28	7.27	17.09	0.00	0.01	0.62	3.35	10.75	24.28
	540	0.00	0.00	0.34	1.83	5.16	8.98	0.00	0.00	0.05	0.27	7.51	14.16	0.00	0.01	0.61	3.25	11.63	20.23
	1080	0.00	0.00	0.33	1.78	5.26	7.59	0.00	0.00	0.05	0.26	8.06	12.35	0.00	0.01	0.59	3.15	12.86	18.00
	5400	0.00	0.00	0.26	1.44	5.21	6.27	0.00	0.00	0.04	0.21	8.40	10.56	0.00	0.01	0.47	2.53	13.28	15.59
ρ_6	30	0.00	0.00	0.16	0.93	–	21.19	0.00	0.00	0.12	0.69	–	30.23	0.00	0.00	0.02	0.14	–	55.91
	90	0.00	0.00	0.15	0.82	3.57	13.47	0.00	0.00	0.11	0.62	4.80	21.92	0.00	0.00	0.02	0.13	9.42	56.61
	270	0.00	0.00	0.15	0.80	4.70	10.23	0.00	0.00	0.11	0.60	7.29	17.15	0.00	0.00	0.02	0.13	18.20	57.73
	540	0.00	0.00	0.14	0.78	3.89	7.65	0.00	0.00	0.11	0.59	7.49	14.18	0.00	0.00	0.02	0.13	23.07	58.32
	1080	0.00	0.00	0.14	0.76	3.15	5.65	0.00	0.00	0.10	0.57	8.02	12.33	0.00	0.00	0.02	0.12	26.41	58.68
	5400	0.00	0.00	0.11	0.62	1.70	2.81	0.00	0.00	0.08	0.47	8.36	10.54	0.00	0.00	0.04	0.06	28.46	58.65
ρ_7	30	0.00	0.00	0.06	0.36	–	16.04	0.00	0.00	0.12	0.67	–	25.37	0.00	0.00	0.04	0.24	–	37.39
	90	0.00	0.00	0.06	0.35	3.68	14.44	0.00	0.00	0.12	0.64	4.81	21.99	0.00	0.00	0.04	0.24	6.74	37.87
	270	0.00	0.00	0.06	0.34	4.81	11.00	0.00	0.00	0.11	0.62	7.30	17.21	0.00	0.00	0.04	0.23	13.17	38.64
	540	0.00	0.00	0.06	0.33	3.93	8.25	0.00	0.00	0.11	0.60	7.49	14.24	0.00	0.00	0.04	0.23	16.77	38.99
	1080	0.00	0.00	0.06	0.33	3.15	6.12	0.00	0.00	0.10	0.58	8.03	12.41	0.00	0.00	0.04	0.21	19.31	39.18
	5400	0.00	0.00	0.06	0.20	1.57	3.01	0.00	0.00	0.09	0.48	8.35	10.62	0.00	0.00	0.00	0.14	20.76	38.87
B_T^8	30	0.00	0.00	0.02	0.11	–	0.46	0.00	0.00	0.05	0.26	–	0.34	0.00	0.00	0.00	0.00	–	0.00
	90	0.00	0.00	0.02	0.10	0.07	0.46	0.00	0.00	0.05	0.26	0.07	0.34	0.00	0.00	0.00	0.00	0.00	0.00
	270	0.00	0.00	0.02	0.11	0.14	0.46	0.00	0.00	0.05	0.25	0.14	0.34	0.00	0.00	0.00	0.00	0.00	0.00
	540	0.00	0.00	0.03	0.12	0.17	0.46	0.00	0.00	0.04	0.25	0.19	0.34	0.00	0.00	0.00	0.00	0.00	0.00
	1080	0.00	0.00	0.03	0.13	0.18	0.46	0.00	0.00	0.04	0.25	0.24	0.34	0.00	0.00	0.00	0.00	0.00	0.00
	5400	0.00	0.00	0.02	0.09	0.16	0.43	0.00	0.00	0.03	0.19	0.27	0.34	0.00	0.00	0.00	0.00	0.00	0.00
B_T^9	30	0.00	0.00	0.02	0.12	–	0.52	0.00	0.00	0.04	0.22	–	0.34	0.00	0.00	0.00	0.00	–	0.00
	90	0.00	0.00	0.02	0.11	0.07	0.51	0.00	0.00	0.04	0.22	0.06	0.34	0.00	0.00	0.00	0.00	0.00	0.00
	270	0.00	0.00	0.02	0.10	0.12	0.51	0.00	0.00	0.03	0.22	0.12	0.34	0.00	0.00	0.00	0.00	0.00	0.00
	540	0.00	0.00	0.02	0.10	0.14	0.50	0.00	0.00	0.02	0.23	0.17	0.34	0.00	0.00	0.00	0.00	0.00	0.00
	1080	0.00	0.00	0.03	0.11	0.14	0.50	0.00	0.00	0.02	0.24	0.24	0.35	0.00	0.00	0.00	0.00	0.00	0.00
	5400	0.00	0.00	0.02	0.09	0.12	0.48	0.00	0.00	0.02	0.21	0.32	0.36	0.00	0.00	0.00	0.00	0.00	0.00

Figs. S1–S13 in the supplemental file show the changes of MPE and MME in all above surface parameters with different topographic approximation methods, which are the illustrations of Tables II–IV and Tables S1–S3.

E. Parameter and Topographic Method Sensitivities With Terrain Condition

It can tell that topography has varied influences on different surface parameters from the above analyses. These differences

TABLE III

MEAN PERCENTAGE ERRORS (MPE, IN%) IN THE SURFACE BROADBAND ALBEDO (α), BROADBAND HEMISPHERICAL EMISSIVITY (ε), NET RADIATION (E_n, IN %), SLOPE DOWNWARD RADIATION (E_d), AND APAR OVER THE MOUNTAINS OF THE STUDY AREA (LOWER TRIANGLE PART). RES IS THE SPATIAL RESOLUTION IN METER. A NUMBER IN BLUE INDICATE THAT THE CORRESPONDING APPROXIMATION METHOD IS ACCEPTABLE (MPE <= 0.1%), WHILE THE RED COLOR REPRESENTS THAT THE ACCURACY OF THE CORRESPONDING METHOD IS BEYOND THE THRESHOLD (MPE > 0.1%)

	Res	Vegetation						Soil						Snow					
		L2	L1	L0	tvf	solo	flat	L2	L1	L0	tvf	solo	flat	L2	L1	L0	tvf	solo	flat
α	30	0.00	0.00	0.22	1.28	–	35.05	0.00	0.00	0.05	0.30	–	42.10	0.00	0.01	0.33	1.82	–	43.78
	90	0.00	0.00	0.22	1.19	6.70	31.59	0.00	0.00	0.05	0.28	7.59	37.92	0.00	0.01	0.32	1.68	7.90	39.29
	270	0.00	0.00	0.21	1.14	13.92	28.19	0.00	0.00	0.05	0.26	15.19	32.64	0.00	0.01	0.30	1.53	15.54	33.37
	540	0.00	0.00	0.21	1.11	17.77	26.62	0.00	0.00	0.05	0.25	19.16	30.08	0.00	0.01	0.28	1.45	19.47	30.48
	1080	0.00	0.00	0.20	1.07	20.72	25.68	0.00	0.00	0.04	0.24	22.31	28.58	0.00	0.01	0.27	1.39	22.70	28.83
	5400	0.00	0.00	0.16	0.84	22.16	23.60	0.00	0.00	0.03	0.19	23.65	25.74	0.00	0.00	0.20	1.07	24.11	25.85
ε	30	0.00	0.00	0.01	0.04	–	13.99	0.00	0.00	0.02	0.13	–	13.96	0.00	0.00	0.00	0.00	–	13.99
	90	0.00	0.00	0.01	0.04	2.99	13.87	0.00	0.00	0.02	0.12	2.99	13.84	0.00	0.00	0.00	0.00	2.99	13.87
	270	0.00	0.00	0.01	0.04	7.23	13.69	0.00	0.00	0.02	0.12	7.22	13.66	0.00	0.00	0.00	0.00	7.23	13.69
	540	0.00	0.00	0.01	0.04	9.60	13.55	0.00	0.00	0.02	0.12	9.58	13.52	0.00	0.00	0.00	0.00	9.60	13.55
	1080	0.00	0.00	0.01	0.04	11.36	13.40	0.00	0.00	0.02	0.11	11.34	13.38	0.00	0.00	0.00	0.00	11.36	13.40
	5400	0.00	0.00	0.01	0.03	12.50	12.76	0.00	0.00	0.02	0.09	12.47	12.74	0.00	0.00	0.00	0.00	12.49	12.76
E_n	30	0.00	0.00	0.24	1.39	–	6.14	0.00	0.00	0.20	1.16	–	3.41	0.00	0.00	0.38	2.27	–	40.87
	90	0.00	0.00	0.24	1.36	1.40	6.17	0.00	0.00	0.20	1.14	0.78	3.43	0.00	0.00	0.37	2.16	11.98	40.97
	270	0.00	0.00	0.24	1.34	3.21	6.17	0.00	0.00	0.20	1.13	1.75	3.41	0.00	0.00	0.35	2.02	24.04	42.29
	540	0.00	0.00	0.24	1.32	4.27	6.18	0.00	0.00	0.20	1.11	2.32	3.40	0.00	0.00	0.34	1.93	31.21	43.60
	1080	0.00	0.00	0.23	1.28	5.04	6.17	0.00	0.00	0.19	1.08	2.74	3.39	0.00	0.00	0.34	1.84	36.54	44.50
	5400	0.00	0.00	0.19	1.05	5.63	5.96	0.00	0.00	0.16	0.88	3.06	3.25	0.00	0.00	0.28	1.50	41.23	44.68
E_d	30	0.00	0.00	0.31	1.79	–	28.77	0.00	0.00	0.24	1.42	–	28.85	0.00	0.01	0.67	3.80	–	28.39
	90	0.00	0.00	0.31	1.74	6.10	26.58	0.00	0.00	0.24	1.37	6.09	26.65	0.00	0.01	0.66	3.69	6.15	26.21
	270	0.00	0.00	0.30	1.67	10.52	22.10	0.00	0.00	0.24	1.32	10.54	22.17	0.00	0.01	0.65	3.55	10.43	21.72
	540	0.00	0.00	0.29	1.63	11.94	19.26	0.00	0.00	0.23	1.29	11.99	19.33	0.00	0.01	0.64	3.46	11.71	18.86
	1080	0.00	0.00	0.28	1.57	13.33	17.65	0.00	0.00	0.22	1.24	13.39	17.72	0.00	0.01	0.61	3.35	13.04	17.25
	5400	0.00	0.00	0.23	1.26	13.81	15.70	0.00	0.00	0.18	0.99	13.86	15.76	0.00	0.01	0.49	2.71	13.50	15.39
APAR	30	0.00	0.00	0.03	0.19	–	26.01	–	–	–	–	–	–	–	–	–	–	–	–
	90	0.00	0.00	0.03	0.18	5.87	23.76	–	–	–	–	–	–	–	–	–	–	–	–
	270	0.00	0.00	0.03	0.18	10.99	21.05	–	–	–	–	–	–	–	–	–	–	–	–
	540	0.00	0.00	0.03	0.17	13.31	19.56	–	–	–	–	–	–	–	–	–	–	–	–
	1080	0.00	0.00	0.03	0.17	15.09	18.69	–	–	–	–	–	–	–	–	–	–	–	–
	5400	0.00	0.00	0.02	0.13	15.80	17.16	–	–	–	–	–	–	–	–	–	–	–	–

TABLE IV

MEAN PERCENTAGE ERRORS (MPE, IN%) IN F_o AND F_e AT 760 nm OVER THE MOUNTAINS OF THE STUDY AREA (LOWER TRIANGLE PART). RES IS THE SPATIAL RESOLUTION IN METER. A NUMBER IN BLUE INDICATE THAT THE CORRESPONDING APPROXIMATION METHOD IS ACCEPTABLE (MPE <= 0.1%), WHILE THE RED COLOR REPRESENTS THAT THE ACCURACY OF THE CORRESPONDING METHOD IS BEYOND THE THRESHOLD (MPE > 0.1%)

	Res	L2	L1	L0	tvf	solo	flat
F_o	30	0.00	0.00	0.03	0.16	–	14.94
	90	0.00	0.00	0.03	0.15	3.39	13.16
	270	0.00	0.00	0.03	0.15	4.88	10.40
	540	0.00	0.00	0.03	0.15	4.71	8.47
	1080	0.00	0.00	0.02	0.14	4.69	7.17
	5400	0.00	0.00	0.02	0.13	4.55	5.85
F_e	30	0.00	0.00	0.03	0.17	–	27.08
	90	0.00	0.00	0.03	0.17	6.00	24.49
	270	0.00	0.00	0.03	0.16	11.13	21.48
	540	0.00	0.00	0.03	0.16	13.42	19.87
	1080	0.00	0.00	0.03	0.16	15.19	18.93
	5400	0.00	0.00	0.02	0.14	15.88	17.33

are closely linked with terrain conditions. Although there are many quantitative indexes, such as slope and terrain ruggedness index [69], we found that SVF well represents the degree of topographic influences. The results are shown in Fig. 8. MPEs induced by different topographic approximation methods with SVF values are analyzed over the entire study area at the 90-m resolution. Fig. 8 shows that the errors caused by topographic approximation methods generally increase with decreasing SVF, but the decreasing patterns differ in different parameters. Fig. 8 tells us the same findings as the above analyses. For example, the flat-surface and solo-slope assumptions are inaccurate for all parameters. The errors induced by these two assumptions are still significant, even SVF closes to 1.0. However, this quantitative analysis gives us more information: ignoring adjacent contributions generally will not induce substantial errors (<1%) for SVF > 0.8 over the study area. This information provides a compromise between accuracy and computational efficiency. Nonetheless, it worth mentioning that using one iteration to include adjacent contributions is a better choice if accuracy is the priority.

IV. DISCUSSION

It can be seen from Section III that influences of topography vary in different surface parameters and different spatial scales. Correspondingly, errors induced by different topographic approximation methods are also different. In general, from the perspective of calculating speed, the flat-surface assumption is the fastest among those methods because

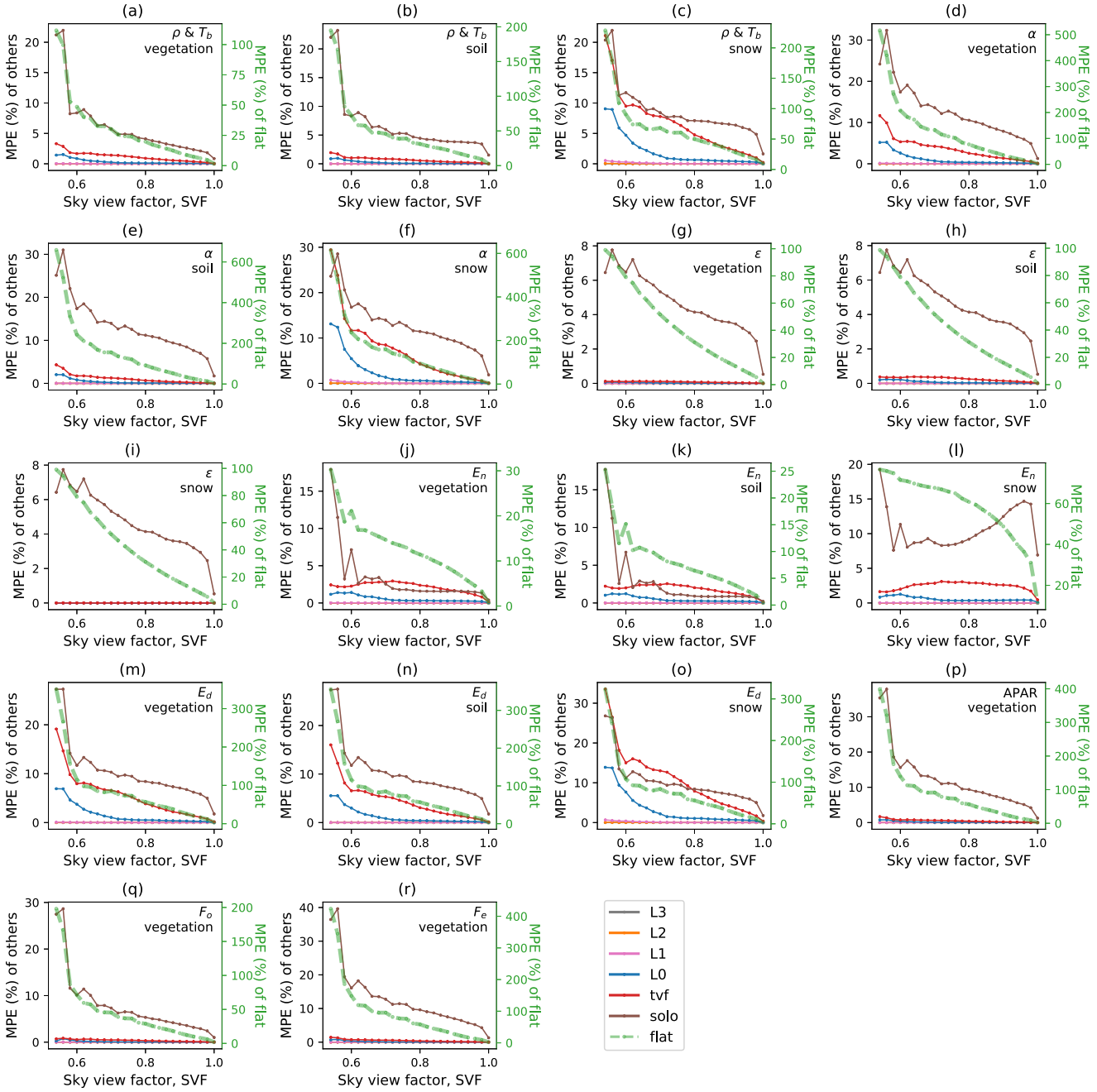

Fig. 8. Change in the MPE induced by different topographic assumptions with SVF over the entire research area. Statistical results are obtained from the 90-m resolution data. (a)–(c) Averaged MPE of nine Landsat-8 bands (reflectance for bands 1–7 and brightness temperature for bands 8 and 9) over vegetation, soil, and snow, respectively. (d)–(f) Surface albedo, α. (g)–(i) Surface emissivity, ε. (j)–(l) Surface net radiation, E_n. (m)–(o) Slope download radiation, E_d. (p) APAR. (q) Observed SIF, F_o. (r) Total emitted SIF, F_e. The right axes are for the MPE of flat-surface assumption, and the left axes are for other topographic approximation methods.

it does not deal with any terrain calculations at all. The next is the solo-slope assumption because no within-pixel calculations are needed. The third one is the L0 method, in which a fine-resolution DEM is used. It does not consider adjacent contributions at all; thus, it avoids the calculation of pixel–pixel interactions within the search radius, which is computationally expensive for fine-scale data. Then is the TVF method, which includes adjacent contributions but approximates surrounding topographies and radiation fluxes to avoid the calculation of pixel–pixel interactions. The final is the Lj ($j > 0$) methods that calculate adjacent contributions through pixel–pixel interactions over fine-scale DEM pixels. However, as demonstrated in Section III, both the flat-surface and solo-slope approximation methods are inaccurate, with induced errors being much larger than 1%. The flat-surface assumption does not consider the influences of topography at all; thus, it is obviously not suitable for mountain areas because, as summarized in Section I, topography can greatly change the radiation received/emitted by a pixel. The solo-slope assumption uses a single slope and aspect value to replace the terrain conditions within a pixel. It neglects within-pixel interactions that play a crucial role in rugged terrains.

This is also why the error induced by the solo-slope approximation method increases with decreasing of spatial resolution. Although the TVF method tries to simulate adjacent contributions, it introduces more uncertainties instead, as demonstrated in the tables of Section III. The reason is that the surrounding topographies and radiation fluxes for a pixel cannot be simply replaced by averaged values. As shown in Fig. 1, the pixel–pixel interactions are influenced by many factors (e.g., slope, aspect, elevation, and visibility). Therefore, the TVF method does not provide a good strategy for calculating adjacent contributions, especially where great topographic relief exists. Also, considering it takes a longer computational time than the L0 method, the TVF method may not be a good choice. The L0 method is preferred if adjacent contributions are not significant. As we can see from the statistics, it actually has quite good accuracy compared to the benchmark. However, at least one iteration (the L1 method) should be used over highly reflective surfaces (e.g., snow surface at visible spectrum) or in areas with deep valleys (e.g., the valley in Fig. 4) to achieve an error of less than 0.1%. Two iterations are needed in the worst case scenarios, which only happen over snow surfaces when using fine-resolution (30–270 m) data in this study. Taking more iterations is not meaningful since it requires more time and does not improve accuracy too much.

This study focuses on building surface models and analyzing the influences of topography on surface parameters; thus, the atmospheric effects are not incorporated. Particularly, the impact of the atmosphere between the target pixel and adjacent pixels has not been simulated in this study. The atmosphere between two pixels affects terrain radiation, such as attenuation of the radiation and the atmospheric path radiation. These effects complicate current models because RT modeling between two pixels is needed, and atmospheric variables, such as horizontal visibility, air temperature, and water vapor content, are needed. However, these parameters are not easy to obtain at the pixel scale, especially at a fine-resolution scale [13]. Besides, accurate modeling of terrain radiation is time-consuming for fine-resolution data. Therefore, the atmospheric effects are not currently modeled considering these complexities and the objectives of this study, but the findings of topographic effects on surface parameters will not be affected.

All the pixels in the study area are assumed to be identical, except in their topography, during simulations. This assumption helps identify the influences caused by topography alone. However, the actual scene is much more complicated. The reflective and emissive properties of solo slopes within a composite slope are usually different. Moreover, these solo slopes can be associated with varying land covers, and even the BOA irradiance may differ within a coarse-scale pixel. In summary, the influence of topography is coupled with surface and atmospheric characterizations. Therefore, more effort is needed when applying this study's models to practical scenarios.

Another factor that needs to be considered is efficiency. As discussed and demonstrated in Section III, terrain radiation contributions need to be modeled under certain conditions. Although one iteration is accurate enough in the vast majority of cases, this process can still be computationally expensive. Calculating topographic variables between a target pixel and its surrounding pixels and saving them in advance is a potential strategy, but this requires substantial storage spaces. Massive computer random access memory (RAM) is also required when considering adjacent contributions.

The finest spatial resolution used in this study is 30-m due to the availability of DEM datasets and computational resources. However, current commercial satellite observations already have better spatial resolutions. Considering that topography has a larger influence with increasing spatial resolution, finer DEM datasets are needed [70]. In addition, increases in spatial resolution demand more RAM and computational time.

Finally, this study analyzes topographic effects on multi-scale parameters from the perspective of forward modeling. It would be more complex when applying the composite-slope models to parameter retrievals. Designing a good retrieval strategy is essential, and a new topographic approximation method with both high accuracy and computational efficiency will probably be needed. Besides, how to validate surface parameters at composite-slope scales is also a problem [71]. Studies on these topics are still at the early stage, which needs to be deeply explored in the future.

V. Conclusion

This study explores topographic effects on surface reflectance, directional brightness temperature, surface net radiation, slope downward radiation, APAR, SIF, broadband albedo, and broadband hemispherical emissivity at a series of spatial resolutions (30, 90, 270, 540, 1080, and 5400 m). Different topographic approximation methods are tested for vegetated, soil, and snow surfaces. The test results demonstrate the following in applications to rugged areas.

1) Topography has varied influences on surface parameters at different spatial resolutions. In general, topographic effects on surface parameters decrease with increasing pixel size, which means that topography is less influential on coarse-scale data than fine-scale data.
2) The assumptions of a flat surface or solo slope induce significant errors in all parameters. This means that a fine-resolution DEM dataset is needed regardless of the spatial resolution of target parameters. The TVF method does not provide a good estimate in adjacent contributions, and its error is even larger than that not considering adjacent contributions at all.
3) The adjacent contribution (i.e., terrain radiation) can be neglected for reflectance at low-reflective bands/areas and broadband hemispherical emissivity. It can also be ignored for the estimation of albedo over low-reflective areas when using coarse spatial resolution data. In addition, neglecting terrain radiation does not induce significant errors in APAR and SIF.
4) The adjacent contribution should be considered for reflectance at high-reflective bands/areas, brightness temperature at low-emissivity bands/areas, surface net radiation, and slope downward radiation. This contribution is also significant for albedo estimations when using fine-resolution data (e.g., 30–270 m) or over

snow surfaces. Nonetheless, one iteration is accurate enough to account for adjacent contributions in the vast of situations, except over snow surface when estimating fine-scale (30–270 m) surface downwelling radiation, in which two iterations are preferred. More iterations do not add value as the iteration process is time-consuming.

These conclusions provide references for those interested in estimating relevant surface parameters over mountain areas, and the solo-slope and composite-slope models provided in this study are ready to use. Future studies will focus on incorporating atmospheric effects into the current models.

ACKNOWLEDGMENT

The authors are grateful to the U.S. Geological Survey (USGS) for providing the Advanced Spaceborne Thermal Emission and Reflection Radiometer (ASTER) Global Digital Elevation Model (ASTGTM) data. They also thank the anonymous reviewers for providing helpful comments and suggestions.

REFERENCES

[1] C. Proy, D. Tanré, and P. Y. Deschamps, "Evaluation of topographic effects in remotely sensed data," *Remote Sens. Environ.*, vol. 30, no. 1, pp. 21–32, Oct. 1989.

[2] A. Mousivand, W. Verhoef, M. Menenti, and B. Gorte, "Modeling top of atmosphere radiance over heterogeneous non-Lambertian rugged terrain," *Remote Sens.*, vol. 7, pp. 8019–8044, Jun. 2015.

[3] J. D. Shepherd and J. R. Dymond, "Correcting satellite imagery for the variance of reflectance and illumination with topography," *Int. J. Remote Sens.*, vol. 24, no. 17, pp. 3503–3514, Jan. 2003.

[4] S. Kobayashi and K. Sanga-Ngoie, "The integrated radiometric correction of optical remote sensing imageries," *Int. J. Remote Sens.*, vol. 29, no. 20, pp. 5957–5985, Oct. 2008.

[5] J. Wen *et al.*, "Modeling land surface reflectance coupled BRDF for HJ-1/CCD data of rugged terrain in Heihe river basin, China," *IEEE J. Sel. Topics Appl. Earth Observ. Remote Sens.*, vol. 8, no. 4, pp. 1506–1518, Apr. 2015.

[6] A. E. Lipton, "Effects of slope and aspect variations on satellite surface temperature retrievals and mesoscale analysis in mountainous terrain," *J. Appl. Meteorol.*, vol. 31, no. 3, pp. 255–264, Mar. 1992.

[7] A. Lipton, "Satellite-view biases in retrieved surface temperatures in mountain areas," *Remote Sens. Environ.*, vol. 60, no. 1, pp. 92–100, Apr. 1997.

[8] Y. Wu, N. Wang, Z. Li, A. Chen, Z. Guo, and Y. Qie, "The effect of thermal radiation from surrounding terrain on glacier surface temperatures retrieved from remote sensing data: A case study from Qiyi Glacier, China," *Remote Sens. Environ.*, vol. 231, Sep. 2019, Art. no. 111267.

[9] K. Wang, X. Zhou, J. Liu, and M. Sparrow, "Estimating surface solar radiation over complex terrain using moderate-resolution satellite sensor data," *Int. J. Remote Sens.*, vol. 26, no. 1, pp. 47–58, Jan. 2005.

[10] Y. Chen, A. Hall, and K. N. Liou, "Application of three-dimensional solar radiative transfer to mountains," *J. Geophys. Res.*, vol. 111, no. D21, Nov. 2006, Art. no. D21111.

[11] W.-L. Lee, K. N. Liou, and A. Hall, "Parameterization of solar fluxes over mountain surfaces for application to climate models," *J. Geophys. Res.*, vol. 116, no. D1, Jan. 2011, Art. no. D01101.

[12] G. Yan, T. Wang, Z. Jiao, X. Mu, J. Zhao, and L. Chen, "Topographic radiation modeling and spatial scaling of clear-sky land surface longwave radiation over rugged terrain," *Remote Sens. Environ.*, vol. 172, pp. 15–27, Jan. 2016.

[13] G. Yan, Z.-H. Jiao, T. Wang, and X. Mu, "Modeling surface longwave radiation over high-relief terrain," *Remote Sens. Environ.*, vol. 237, Feb. 2020, Art. no. 111556.

[14] J. G. Wen, Q. Liu, Q. Liu, Q. Xiao, and X. Li, "Scale effect and scale correction of land-surface albedo in rugged terrain," *Int. J. Remote Sens.*, vol. 30, no. 20, pp. 5397–5420, Sep. 2009.

[15] B. Gao, L. Jia, and M. Menenti, "An improved method for retrieving land surface albedo over rugged terrain," *IEEE Geosci. Remote Sens. Lett.*, vol. 11, no. 2, pp. 554–558, Feb. 2014.

[16] F. Gemmell, "An investigation of terrain effects on the inversion of a forest reflectance model," *Remote Sens. Environ.*, vol. 65, no. 2, pp. 155–169, Aug. 1998.

[17] A. Gonsamo and J. Chen, "Improved LAI algorithm implementation to MODIS data by incorporating background, topography, and foliage clumping information," *IEEE Trans. Geosci. Remote Sens.*, vol. 52, no. 2, pp. 1076–1088, Feb. 2014.

[18] P. Zhao, W. J. Fan, Y. Liu, X. H. Mu, X. R. Xu, and J. J. Peng, "Study of the remote sensing model of FAPAR over rugged terrains," *Remote Sens.*, vol. 8, no. 4, p. 309, Apr. 2016.

[19] J. Wen *et al.*, "Characterizing land surface anisotropic reflectance over rugged terrain: A review of concepts and recent developments," *Remote Sens.*, vol. 10, no. 3, p. 370, Feb. 2018.

[20] C. B. Schaaf, X. W. Li, and A. H. Strahler, "Topographic effects on bidirectional and hemispherical reflectances calculated with a geometric-optical canopy model," *IEEE Trans. Geosci. Remote Sens.*, vol. 32, no. 6, pp. 1186–1193, Nov. 1994.

[21] B. Combal, H. Isaka, and C. Trotter, "Extending a turbid medium BRDF model to allow sloping terrain with a vertical plant stand," *IEEE Trans. Geosci. Remote Sens.*, vol. 38, no. 2, pp. 798–810, Mar. 2000.

[22] W. Fan, J. M. Chen, W. Ju, and G. Zhu, "GOST: A geometric-optical model for sloping terrains," *IEEE Trans. Geosci. Remote Sens.*, vol. 52, no. 9, pp. 5469–5482, Sep. 2014.

[23] W. Fan, J. M. Chen, W. Ju, and N. Nesbitt, "Hybrid geometric optical–radiative transfer model suitable for forests on slopes," *IEEE Trans. Geosci. Remote Sens.*, vol. 52, no. 9, pp. 5579–5586, Sep. 2014.

[24] W. Fan, J. Li, and Q. Liu, "GOST2: The improvement of the canopy reflectance model GOST in separating the sunlit and shaded leaves," *IEEE J. Sel. Topics Appl. Earth Observ. Remote Sens.*, vol. 8, no. 4, pp. 1423–1431, Apr. 2015.

[25] G. Yin, A. Li, W. Zhao, H. Jin, J. Bian, and S. Wu, "Modeling canopy reflectance over sloping terrain based on path length correction," *IEEE Trans. Geosci. Remote Sens.*, vol. 55, no. 8, pp. 4597–4609, Aug. 2017.

[26] S. Wu *et al.*, "Modeling discrete forest anisotropic reflectance over a sloped surface with an extended GOMS and SAIL model," *IEEE Trans. Geosci. Remote Sens.*, vol. 57, no. 2, pp. 944–957, Feb. 2019.

[27] H. Shi and Z. Xiao, "The 4SAILT model: An improved 4SAIL canopy radiative transfer model for sloping terrain," *IEEE Trans. Geosci. Remote Sens.*, vol. 59, no. 7, pp. 5515–5525, Jul. 2021.

[28] S. Wu *et al.*, "Characterization of remote sensing albedo over sloped surfaces based on DART simulations and *in situ* observations," *J. Geophys. Res., Atmos.*, vol. 123, no. 16, pp. 8599–8622, Aug. 2018.

[29] J. E. Hay, "Calculating solar radiation for inclined surfaces: Practical approaches," *Renew. Energy*, vol. 3, nos. 4–5, pp. 373–380, Jun. 1993.

[30] C. R. Duguay, "An approach to the estimation of surface net radiation in mountain areas using remote sensing and digital terrain data," *Theor. Appl. Climatol.*, vol. 52, nos. 1–2, pp. 55–68, 1995.

[31] J. E. Sicart, J. W. Pomeroy, R. L. H. Essery, and D. Bewley, "Incoming longwave radiation to melting snow: Observations, sensitivity and estimation in northern environments," *Hydrol. Processes*, vol. 20, no. 17, pp. 3697–3708, 2006.

[32] S. Wu, J. Wen, D. You, H. Zhang, Q. Xiao, and Q. Liu, "Algorithms for calculating topographic parameters and their uncertainties in downward surface solar radiation (DSSR) estimation," *IEEE Geosci. Remote Sens. Lett.*, vol. 15, no. 8, pp. 1149–1153, Aug. 2018.

[33] H. Shi and Z. Xiao, "SIFT: Modeling solar-induced chlorophyll fluorescence over sloping terrain," *IEEE Geosci. Remote Sens. Lett.*, early access, Mar. 30, 2021, doi: 10.1109/LGRS.2021.3067879.

[34] D. Gratton, P. Howarth, and D. Marceau, "Using Landsat-5 thematic mapper and digital elevation data to determine the net radiation field of a mountain glacier," *Remote Sens. Environ.*, vol. 43, no. 3, pp. 315–331, Mar. 1993.

[35] P. Sirguey, "Simple correction of multiple reflection effects in rugged terrain," *Int. J. Remote Sens.*, vol. 30, no. 4, pp. 1075–1081, Feb. 2009.

[36] S. Wu *et al.*, "The definition of remotely sensed reflectance quantities suitable for rugged terrain," *Remote Sens. Environ.*, vol. 225, pp. 403–415, May 2019.

[37] Z.-H. Jiao, G. Yan, T. Wang, X. Mu, and J. Zhao, "Modeling of land surface thermal anisotropy based on directional and equivalent brightness temperatures over complex terrain," *IEEE J. Sel. Topics Appl. Earth Observ. Remote Sens.*, vol. 12, no. 2, pp. 410–423, Feb. 2019.

[38] X. Zhu *et al.*, "Retrieval of land surface temperature with topographic effect correction from Landsat 8 thermal infrared data in mountainous areas," *IEEE Trans. Geosci. Remote Sens.*, vol. 59, no. 8, pp. 6674–6687, Aug. 2021, doi: 10.1109/TGRS.2020.3030900.

[39] Y. Liu, T. Hiyama, and Y. Yamaguchi, "Scaling of land surface temperature using satellite data: A case examination on ASTER and MODIS products over a heterogeneous terrain area," *Remote Sens. Environ.*, vol. 105, no. 2, pp. 115–128, Nov. 2006.
[40] M. D. Müller and D. Scherer, "A grid- and subgrid-scale radiation parameterization of topographic effects for mesoscale weather forecast models," *Monthly Weather Rev.*, vol. 133, no. 6, pp. 1431–1442, Jun. 2005.
[41] R. Essery and D. Marks, "Scaling and parametrization of clear-sky solar radiation over complex topography," *J. Geophys. Res., Atmos.*, vol. 112, no. D10, May 2007, Art. no. D10122.
[42] N. Helbig and H. Löwe, "Shortwave radiation parameterization scheme for subgrid topography," *J. Geophys. Res., Atmos.*, vol. 117, no. D3, Feb. 2012, Art. no. D03112.
[43] D. Hao *et al.*, "Modeling anisotropic reflectance over composite sloping terrain," *IEEE Trans. Geosci. Remote Sens.*, vol. 56, no. 7, pp. 3903–3923, Jul. 2018.
[44] D. Hao, J. Wen, Q. Xiao, D. You, and Y. Tang, "An improved topography-coupled kernel-driven model for land surface anisotropic reflectance," *IEEE Trans. Geosci. Remote Sens.*, vol. 58, no. 4, pp. 2833–2847, Apr. 2020.
[45] R. Richter, "Correction of atmospheric and topographic effects for high spatial resolution satellite imagery," *Int. J. Remote Sens.*, vol. 18, no. 5, pp. 1099–1111, Mar. 1997.
[46] S. Sandmeier and K. I. Itten, "A physically-based model to correct atmospheric and illumination effects in optical satellite data of rugged terrain," *IEEE Trans. Geosci. Remote Sens.*, vol. 35, no. 3, pp. 708–717, May 1997.
[47] R. Richter, "Correction of satellite imagery over mountainous terrain," *Appl. Opt.*, vol. 37, no. 18, pp. 4004–4015, Jun. 1998.
[48] R. Richter and D. Schläpfer, "Geo-atmospheric processing of airborne imaging spectrometry data. Part 2: Atmospheric/topographic correction," *Int. J. Remote Sens.*, vol. 23, no. 13, pp. 2631–2649, Jan. 2002.
[49] L. Guanter, R. Richter, and H. Kaufmann, "On the application of the MODTRAN4 atmospheric radiative transfer code to optical remote sensing," *Int. J. Remote Sens.*, vol. 30, no. 6, pp. 1407–1424, Mar. 2009.
[50] J. Wen, Q. Liu, Q. Liu, Q. Xiao, and X. Li, "Parametrized BRDF for atmospheric and topographic correction and albedo estimation in Jiangxi rugged terrain, China," *Int. J. Remote Sens.*, vol. 30, no. 11, pp. 2875–2896, Jun. 2009.
[51] F. Q. Li *et al.*, "A physics-based atmospheric and BRDF correction for Landsat data over mountainous terrain," *Remote Sens. Environ.*, vol. 124, pp. 756–770, Sep. 2012.
[52] S. Vanonckelen, S. Lhermitte, and A. Van Rompaey, "The effect of atmospheric and topographic correction methods on land cover classification accuracy," *Int. J. Appl. Earth Observ. Geoinf.*, vol. 24, pp. 9–21, Oct. 2013.
[53] F. Santini and A. Palombo, "Physically based approach for combined atmospheric and topographic corrections," *Remote Sens.*, vol. 11, no. 10, p. 1218, May 2019.
[54] C. E. Woodcock and A. H. Strahler, "The factor of scale in remote sensing," *Remote Sens. Environ.*, vol. 21, no. 3, pp. 311–332, Apr. 1987.
[55] H. Jin, A. Li, W. Xu, Z. Xiao, J. Jiang, and H. Xue, "Evaluation of topographic effects on multiscale leaf area index estimation using remotely sensed observations from multiple sensors," *ISPRS J. Photogramm. Remote Sens.*, vol. 154, pp. 176–188, Aug. 2019.
[56] H. Jin *et al.*, "A multiscale assimilation approach to improve fine-resolution leaf area index dynamics," *IEEE Trans. Geosci. Remote Sens.*, vol. 57, no. 10, pp. 8153–8168, Oct. 2019.
[57] H. Shi, Z. Xiao, J. Wen, and S. Wu, "An optical-thermal surface-atmosphere radiative transfer model coupling framework with topographic effects," *IEEE Trans. Geosci. Remote Sens.*, early access, Dec. 24, 2021, doi: 10.1109/TGRS.2020.3044061.
[58] C. L. Walthall, J. M. Norman, J. M. Welles, G. Campbell, and B. L. Blad, "Simple equation to approximate the bidirectional reflectance from vegetative canopies and bare soil surfaces," *Appl. Opt.*, vol. 24, no. 3, pp. 383–387, Feb. 1985.
[59] A. A. Kokhanovsky and F.-M. Breon, "Validation of an analytical snow BRDF model using PARASOL multi-angular and multispectral observations," *IEEE Geosci. Remote Sens. Lett.*, vol. 9, no. 5, pp. 928–932, Sep. 2012.
[60] W. Verhoef, L. Jia, Q. Xiao, and Z. Su, "Unified optical-thermal four-stream radiative transfer theory for homogeneous vegetation canopies," *IEEE Trans. Geosci. Remote Sens.*, vol. 45, no. 6, pp. 1808–1822, Jun. 2007.
[61] C. van der Tol, W. Verhoef, J. Timmermans, A. Verhoef, and Z. Su, "An integrated model of soil-canopy spectral radiances, photosynthesis, fluorescence, temperature and energy balance," *Biogeosciences*, vol. 6, no. 12, pp. 3109–3129, Dec. 2009.
[62] S. G. Warren and R. E. Brandt, "Optical constants of ice from the ultraviolet to the microwave: A revised compilation," *J. Geophys. Res.*, vol. 113, no. D14, Jul. 2008, Art. no. D14220.
[63] J. Dozier and J. Frew, "Rapid calculation of terrain parameters for radiation modeling from digital elevation data," *IEEE Trans. Geosci. Remote Sens.*, vol. 28, no. 5, pp. 963–969, Sep. 1990.
[64] W. Verhoef and H. Bach, "Coupled soil-leaf-canopy and atmosphere radiative transfer modeling to simulate hyperspectral multi-angular surface reflectance and TOA radiance data," *Remote Sens. Environ.*, vol. 109, no. 2, pp. 166–182, Jul. 2007.
[65] H. Shi, Z. Xiao, S. Liang, and X. Zhang, "Consistent estimation of multiple parameters from MODIS top of atmosphere reflectance data using a coupled soil-canopy-atmosphere radiative transfer model," *Remote Sens. Environ.*, vol. 184, pp. 40–57, Oct. 2016.
[66] H. Fujisada, M. Urai, and A. Iwasaki, "Technical methodology for ASTER global DEM," *IEEE Trans. Geosci. Remote Sens.*, vol. 50, no. 10, pp. 3725–3736, Oct. 2012.
[67] B. Horn, "Hill shading and the reflectance map," *Proc. IEEE*, vol. 69, no. 1, pp. 14–47, Jan. 1981.
[68] J. Dozier, J. Bruno, and P. Downey, "A faster solution to the horizon problem," *Comput. Geosci.*, vol. 7, no. 2, pp. 145–151, Jan. 1981.
[69] S. J. Riley, S. D. DeGloria, and R. Elliot, "A terrain ruggedness index that quantifies topographic heterogeneity," *Intermountain J. Sci.*, vol. 5, nos. 1–4, pp. 23–27, Dec. 1999.
[70] S. T. Arundel, C.-A. M. Archuleta, L. A. Phillips, B. L. Roche, and E. W. Constance, "1-meter digital elevation model specification," US Geol. Surv., Reston, VA, USGS Numbered Series, Tech. Rep. 11-B7, 2015, doi: 10.3133/tm11B7.
[71] G. Yan *et al.*, "An operational method for validating the downward shortwave radiation over rugged terrains," *IEEE Trans. Geosci. Remote Sens.*, vol. 59, no. 1, pp. 714–731, Jan. 2021.

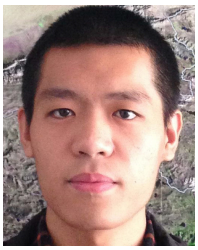

Hanyu Shi (Student Member, IEEE) received the B.S. and M.S. degrees from Beijing Normal University, Beijing, China, in 2014 and 2017, respectively, where he is pursuing the Ph.D. degree.

His research interests include radiative transfer and estimation of surface variables.

Zhiqiang Xiao (Member, IEEE) received the Ph.D. degree in geophysical prospecting and information technology from Central South University, Changsha, China, in 2004.

From 2004 to 2006, he was a Post-Doctoral Research Associate with Beijing Normal University, Beijing, China, where he is a Professor with the Faculty of Geographical Science. His research interests include retrieval of land biophysical parameters from remotely sensed data and assimilating radiometric observations into dynamic models.